Master's thesis

NTNU
Norwegian University of Science and Technology
Faculty of Engineering
Department of Mechanical and Industrial Engineering

Sondre Olsøybakk Kolstad

Structural Integrity of AISI 316L Fabricated via Material Extrusion Additive Manufacturing

Master's thesis in Material Science and Engineering
Supervisor: Seyed Mohammed Javad Razavi
Co-supervisor: Saveria Spiller
June 2022

NTNU
Kunnskap for en bedre verden

Sondre Olsøybakk Kolstad

Structural Integrity of AISI 316L Fabricated via Material Extrusion Additive Manufacturing

Master's thesis in Material Science and Engineering
Supervisor: Seyed Mohammed Javad Razavi
Co-supervisor: Saveria Spiller
June 2022

Norwegian University of Science and Technology
Faculty of Engineering
Department of Mechanical and Industrial Engineering

NTNU
Norwegian University of
Science and Technology

Preface

This master's thesis is submitted as a final deliverable for a master's degree in Material Science and Engineering at the Norwegian University of Science and Technology. It was conducted at the Department of Mechanical and Industrial Engineering under the supervision of Professor Seyed Mohammed Javad Razavi and Ph.D. Candidate Saveria Spiller.

The thesis is a continuation of my specialization project in TMM4560, which was submitted on 13th of December 2021. After the submission of the thesis, further work related to the topic will be conducted by Saveria Spiller for her Ph.D.

I would like to thank my supervisor Seyed Mohammed Javad Razavi for guidance, helpful feedback, and valuable support throughout the year. I would thank Zhuo Xu 'Loker' for helping me with troubleshooting and instructions at the laboratory. Finally, I would like to give a huge thanks to my co-supervisor, Saveria Spiller, who has spent countless hours with me at the laboratory to assist with experiments and generally forming the thesis. The thesis would not be in this state without your knowledge, patience, rapid feedback, and general eagerness to help.

Trondheim 11th of June 2022

Sondre Olsøybakk Kolstad

Abstract

Additive manufacturing is an excellent method of producing complex geometries with various materials. Generally, steel components are manufactured for high-strength applications due to their high strength and fatigue resistance. Additive manufacturing of steel components is primarily conducted using advanced equipment such as selective laser melting, selective laser sintering, and electron beam melting. However, these manufacturing methods are expensive in terms of the initial cost of the equipment and the production cost.

The thesis discusses the possibility of using fused deposition modeling with sintering to manufacture specimens with minimal loss in mechanical properties. The procedure is conducted using a composite filament of AISI 316L particles and a polymer binder. This manufacturing method requires post-processing treatment such as debinding and sintering to remove the binder and initiate densification of the steel specimens. Initially, experimentation of printing parameters is performed to obtain excellent specimens and to eliminate defects that may affect the mechanical properties. After post-processing treatment, tensile and fatigue tests are performed with the solid AISI 316L specimens. Using a scanning electron microscope to analyze the fracture surfaces, information such as the number and size of defects, pore distribution, and grain size is obtained. Moreover, the microstructure analysis is used to explain the mechanical data and discuss future modifications to improve the properties.

Sammendrag

Additiv produksjon er en utmerket metode for å produsere komplekse geometrier med forskjellige materialer. Generelt er stålkomponenter produsert for høystyrke-applikasjoner på grunn av deres høye styrke og evne til å motstå utmatting. Additiv produksjon av stålkomponenter utføres primært ved bruk av avansert utstyr som selektiv lasersmelting, selektiv lasersintring og elektronstrålesmelting. Likevel er disse produksjonsmetodene dyre når det gjelder utstyrskostnaden og produksjonskostnaden.

Oppgaven diskuterer muligheten for å bruke smeltet deponeringsmodellering med sintring for å produsere prøver med minimalt tap i mekaniske egenskaper. Prosedyren utføres ved bruk av et kompositttfilament bestående av AISI 316L-partikler og et polymerbindemiddel. Denne produksjonsmetoden krever etterbehandling som avbinding og sintring for å fjerne bindemiddelet og iverksette fortetting av stålprøvene. Til å begynne med utføres eksperimentering av printeparametere for å oppnå utmerkede prøver og for å eliminere defekter som kan påvirke de mekaniske egenskapene. Etter avbinding og sintring utføres strekk- og utmattingstester med de solide AISI 316L-prøvene. Ved å bruke et sveipelektronmikroskop for å analysere bruddflatene, får man informasjon som antall og størrelse på defekter, porefordeling og kornstørrelse. Dessuten brukes mikrostrukturanalysen til å forklare de mekaniske dataene og diskutere fremtidige modifikasjoner for å forbedre egenskapene.

Contents

Abbreviations

Abbreviation	Full name
ABS	Acrylonitrile Butadiene Styrene
AM	Additive Manufacturing
CAD	Computer Aided Design
CT specimens	Compact Tension specimens
DIC	Digital Image Correlation
EBM	Electron Beam Melting
FDM	Fused Deposition Modeling
FDMet	Fused Deposition of Metals
FDMS	Fused Deposition Modeling with Sintering
FFF	Fused Filament Fabrication
HCF	High Cycle Fatigue
LCF	Low Cycle Fatigue
LENS	Laser Engineered Net Shaping
LOM	Laminated Object Manufacturing
MIM	Metal Injection Moulding
PLA	Polyactic Acid
POM	Polyformaldehyde
PSD	Particle Size Distribution
SEM	Scanning Electron Microscopy
SLA	Stereolithography
SLM	Selective Laser Melting
SLS	Selective Laser Sintering
STD	Standard Deviation
TPE	Thermoplastic Elastomer
UTS	Ultimate Tensile Strength

List of Tables

List of Figures

1 Introduction

1.1 Background

Some sections are borrowed from the specialization project, which is an introductory study to the thesis.

Additive Manufacturing (AM) is not a new concept but a concept undergoing massive development over the past decades. Nowadays, the name Additive Manufacturing is commonly known as 3D-printing, and it is being used to produce components used in machines, decorations, daily-life products, as well as in medicine and aerospace applications [1]. In the 1980s, a transition from subtractive fabrication to additive fabrication occurred. Subtractive fabrication is the concept of removing material from bulk to form the sought specimen. This procedure results in a considerable amount of waste material that otherwise could have been used for other applications [2].

On the other hand, additive fabrication produces the specimen with little to no waste. In other words, subtractive and additive manufacturing are two opposites regarding the fabrication method. The original idea of additive manufacturing originated from the concept of a regular ink-jet printer, and the development of 3D printers was designed to use similar technologies [2].

Over the past decades, multiple new technologies of AM have been developed that utilize very different fabrication methods. Some examples of additive manufacturing techniques include Stereolithography (SLA), Electron Beam Melting (EBM), Selective Laser Melting (SLM), Selective Laser Sintering (SLS), Laser Engineered Net Shaping (LENS), Laminated Object Manufacturing (LOM), and Fused Deposition Modeling with Sintering (FDMS). Fused deposition modeling is widely used for its energy efficiency and low cost. The specimens are produced by a filament which undergoes heating and layerwise deposition on the bed. Moreover, FDMS is the manufacturing method that will be utilized in this thesis.

Table 1: An overview of common AM techniques for manufacturing specimens [3]. Metal printing with FDMS is only possible in combination with a polymer binder.

Common AM processes		
Acronym	**Process**	**Material**
FDMS	Fused Deposition Modeling with Sintering	Polymer, (metal)
SLA	Stereolithography	Polymer, metal, ceramics, composite
SLM	Selective Laser Melting	Metal
SLS	Selective Laser Sintering	Metal
LOM	Laminated Object Manufacturing	Paper, metal, polymer
LENS	Laser Engineered Net Shaping	Metal
EBM	Electron Beam Melting	Metal

The technological development of electronics and hardware have made it possible to use computational software to solve problems regarding the mechanical behavior of components. Today, software such as SOLIDWORKS and Abaqus can be used to obtain information about a specimen in a given situation without the need for manual calculations, and experiments [2]. As a result, detailed data can be extracted from the software and be used to perform real-life tasks. This way, one can compare both the component's theoretical and practical properties by obtaining simulated and experimental data.

Knowledge about specific printing parameters was obtained from the specialization project, which was an introductory study of additive manufactured steel components using a conventional FDM printer. The project was a great course in the influence of printing parameters and how to manufacture smaller specimens with great surface and infill quality. Although the specimens were small, knowledge about temperatures, printing speeds, and layer heights was particularly useful. The project's purpose was to provide the basic information needed to produce more advanced specimens with higher strength requirements in this thesis.

Terms such as specimens, parts, and green parts may be used on multiple occasions in the thesis to describe the same concept. While specimens and parts are the same, green parts translate to the produced specimens before debinding and sintering. Therefore, it is not valid to use the term green part when discussing specimens post sintering.

1.2 Motivation

Typical metal printing techniques have been known to be very energy consuming and cost expensive. However, using FDMS reduces energy consumption and cost. Still, the specimens are not suited for construction or other high-stress applications after fabrication. This is due to their non-optimal mechanical properties, which need improvement. Printed AISI 316L using FDM does not share the same properties as AISI 316L specimens using conventional production techniques such as casting or extruding. Hence, post-processing treatment should be performed and analyzed to observe its effects on the specimen. Therefore, it is sought to better understand the FDMS process and its implications on the specimen to further develop new techniques and improve the current mechanical properties. Thus, making it a suitable method for high-strength applications.

1.3 Scope of work

The thesis aims to use the specialization project results to print excellent specimens of BASF 316L Ultrafuse. The three optimal printing configurations from the specialization project are used as bases to obtain optimal configurations for printing large specimens. A printing configuration is a set of selected printing parameters that results in optimal specimen quality in terms of surface and infill. The specimen types include tensile specimens, fatigue specimens, and CT specimens. Each specimen type has a specific geometry and is designed in SOLIDWORKS. The specimens, after fabrication, are then sent to an external company for debinding and sintering. After returning, tensile and fatigue testing is performed on the solid AISI 316L specimens to obtain mechanical properties. Initially, the objective was to perform machining and fracture testing on CT specimens. However, it was cut due to time restrictions and technical difficulties with the machining tools in the last phase of the thesis. Still, the debinding and sintering of the CT specimens give valuable information about the shrinkage and mass loss of larger solid specimens. That is not obtained to the same degree by the thinner tensile and fatigue speci-

mens. The procedure of designing the CT specimens for sintering and machining is still explained in the thesis so that it may be continued in future work. Finally, fractography is performed using SEM to analyze the fracture surfaces of the fatigue specimens. Hence, the main goal is to analyze and optimize the printing process to obtain optimal mechanical properties for the FDMS metal specimens.

The experimental procedure of the thesis is divided into several parts in the represented order:

- Designing the tensile, fatigue, and CT specimens according to ASTM standards.
- Performing alterations to the optimal printing configurations from the specialization project to accommodate the larger specimens.
- Printing five tensile specimens, 12 fatigue specimens, and eight CT specimens in three different build orientations.
- Shipping the specimens to an external company for debinding and sintering.
- Measuring shrinkage and mass loss of the specimens before and after debinding and sintering.
- Performing tensile testing of the tensile specimens with DIC and fatigue testing of the fatigue specimens.
- Performing fractography on the fracture surfaces of fatigue specimens using SEM.
- Discussing the results.

2 Theory

Several sections from the specialization project are borrowed in the theory section of the thesis due to their high relevance to the experiments performed.

2.1 General

Forging, casting, machining, extrusion, Metal Injection Moulding (MIM), and substrate fabrication are examples of traditional metal manufacturing techniques. The most common metal production techniques are casting and forging, but they demand much physical labor and leave little room for fine-tuning. Other issues like underfilling the mold and flowability are critical during casting and can fail if not optimized. Machining or deformation of solid metal is also possible. According to [4], one approach is to roll the metal with or without heat, which introduces many surface defects and improves hardness. The thickness of the sheet formed by rolling can be adjusted to reach a specific hardness and microstructure, and it can then be cut to form a shape. Extrusion is also commonly used to extrude a metal through a form to achieve a specific geometry, either with or without heat. This method helps make lengthy, uniform specimens, but it cannot be used to make specimens with different geometries. To process of MIM is comparable to Fused Deposition of Metals (FDMet). Metal powder is injected into a mold using a binder, then debinding and sintering occur. This approach necessitates the creation of a mold for each geometry, and, like FDMet, attaining optimal mechanical characteristics of the specimen remains a significant difficulty [5]. As previously stated, substrate fabrication involves removing material from bulk to create a specimen. Substrate fabrication can provide detailed geometries, but they are costly in terms of production time and material cost.

AM is now widely employed because of the high cost and time advantages, and multiple printing techniques can be used for various applications, materials, and properties. K.S. Prakash et al. [6] investigate various AM approaches, including their functionality, benefits, and drawbacks. Stereolithography (SLA), Selective Laser Sintering (SLS), Selective Laser Melting (SLM), and Laminated Object Manufacturing (LOM) are the terms used to describe these processes. SLA employs a UV laser to polymerize liquid resin layer by layer, with the platform being lowered once each cross-section is done. This process generates excellent surface finishes on specimens, but it is limited in size, cost, and material variety. SLS works by having a bed, the building platform, filled with powdered material inside a chamber heated

to nearly the material's melting point. A CO_2 laser heats the particles in the bed layer by layer while a piston controls the platform's descent. Because the particles are sintered during the printing process, no additional post-processing is required if a metal powder is utilized. Its key advantages are the ability to swiftly manufacture complex parts, a wide range of available materials, the ability to recycle unused powder, and enhanced mechanical qualities compared to other AM processes. However, compared to SLA, the surface finish is not as good. Its precision is highly dependent on particle size, and it must be carried out in an inert atmosphere to avoid oxidation. Finally, a laser bar is used in SLM to liquefy a material, which is subsequently infused into a specific location to make the specimen. The substance cools and solidifies after being infused.

In addition, unlike SLS, SLM requires post-processing treatment to increase its characteristics. This approach works with a wide range of materials and can be used to repair existing parts that would be too expensive or difficult to repair using other methods. One drawback is that considerable residual stresses remain in the specimen after cooling the material, making it unsuitable for several applications. It also produces an uneven surface, which may require further machining. Laser Engineered Net Shaping (LENS) is a hybrid of AM and substrate fabrication in which the material is stacked in thin layers. Pressure, heat, and thermal adhesive coating are utilized to attach the layers, and a laser is used to cut the specimen shape from the substrate. The low cost, wide material range, capacity to produce larger specimens and lack of support structures or post-process treatment make this approach appealing. However, it produces a poor surface finish and limited precision, making it challenging to print specimens with internal cavities. Electron Beam Melting (EBM), which uses a high-power electron beam to melt the material without leaving any residual stresses in the final specimen, is another standard production technology for metal specimens. During printing, the specimen is also held in a vacuum to ensure its purity [7].

As previously stated, FDM is an AM approach that leverages computer 3D geometry to produce physical specimens. Software such as SOLIDWORKS, AutoCAD, and Abaqus can be used to create 3D geometries. FDM produces minimal waste compared to traditional manufacturing methods and may build complicated shapes that would otherwise be hard to duplicate. The material in the form of filament/feedstock, the extruder, the heater, the nozzle, and the bed are the essential components of an FDM printer. The material is forced into the heating chamber with the help of the extruder. The material then melts into a semi-liquid state. As seen in Figure

1, the material is extruded via the nozzle and onto the bed.

The printer constructs the specimen layer by layer in cross-sections. The head moves along the bed in a two-dimensional plane. Then it deposits material according to the computer's 3D geometry's cross-section. The bed descends one layer of thickness when the cross-section is completed, and the process is repeated by depositing new material over the preceding layer. When extruded out of the nozzle, the deposited material acquires the shape of a string, also called a strand. While the substance is still semi-liquid, the strands merge, creating a denser specimen. Support structures are built to eliminate weak spots that could collapse if parts of the specimen have overhang angles below 45°. The support structures can be printed with either the main nozzle or a secondary nozzle if one is available. The second nozzle is typically smaller in diameter than the main nozzle, resulting in constructions with thinner strands. The thinner strands are created to easily remove the support structures after the specimen has been constructed. Manual labor with a knife or abrasive tools can be used to remove the material. Internally, the printing program may be able to manage the amount and pattern of material deposition. The deposition is also influenced by the desired mechanical properties, production time, and material cost. The diameter of the primary nozzle may also be changed to produce a specimen with thinner strands and consequently decreased surface roughness. However, this will lengthen the manufacturing process. Other printing settings, such as printing speed, cooling fan speed, and extrusion rate, can also be adjusted. The bed can be heated, or the specimen can adhere to the bed with glue. The entire specimen can be removed from the building plate and cleaned once formed. P. Dudek [8] in his research study on FDM 3D printing technology explains the process of printing specimens using FDM in great detail.

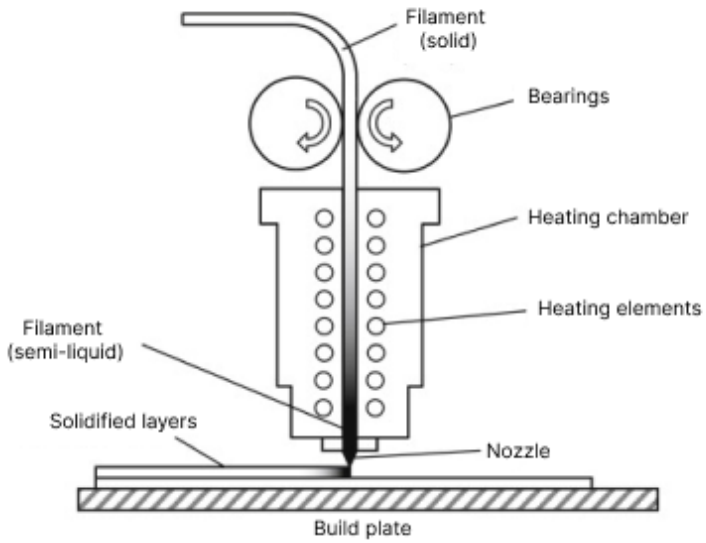

Figure 1: The main components of a regular FDM printer illustrated by Gonzalez-Macia et al. [9]. The extruder moves along the build plate while extruding the semi-liquid material layerwise.

The different extrusion methods for FDM printing are discussed by A.I. Nurhudan et al. [10]. These methods are Screw, Syringe, and Filament-based extrusion. The material for the Syringe-based extrusion method is in the form of a rod. A solid plunger pushes the rod into the heating chamber, where the material undergoes the plasticizing process. The semi-liquid material is pumped via the nozzle and onto the bed to build the specimen. This extrusion procedure can also be performed with a fluid material. With a Screw-based extrusion method, the material is in the form of a granule feedstock. A driving screw pushes the feedstock into the heating chamber and through the nozzle. In the filament-based extrusion process, a feed roller drives a string-formed filament into the heating chamber. The heater then guarantees that the filament exits the nozzle onto the bed in a semi-liquid state. Fused Filament Fabrication (FFF), which refers to FDM with a Filament-based extrusion, is also a popular printing technology for its safety, simplicity, and low component costs. As a result, this is the method of extrusion used in the thesis.

There are various advantages to using metal Fused Deposition Modeling over alternative metal printing techniques, according to Durgun and Ertan [11]. For starters, it works with a wide range of materials. It is also simple to change the material, with low maintenance costs and short lead times for thin components. Furthermore, it can print at lower temperatures, which considerably minimizes the risks associated with high-temperature operations, but at the expense of quality. It does, however, result in rougher surfaces, a longer time to produce thicker parts, and limited di-

mensions. Although metal FDM printing has drawbacks, some can be avoided by changing the printing parameters.

Using a filament with a polymer matrix has proven an excellent composite material for metal printing. FDM printing using metal powders can be performed since the polymer acts as a binder for the metal powder, according to Mohd Pu'ad et al. [12]. The core material, backbone, and additives are the three main components of the binder. The principal material in AISI 316L is commonly a thermoplastic elastomer (TPE) or polyformaldehyde (POM), and it makes up 50-90% of the binder composition [13][14]. Grafted polyolefin, polypropylene, dioctyl phthalate, dibutyl phthalate, or zinc oxide may be used as the backbone. In addition, an additive may be used, which accounts for 0-10% of the final binder system's rheological properties [10]. Due to the flowability of the semi-liquid binder, the metal particles are evenly distributed across the printed specimen. However, this mix must be optimized to get ideal mechanical properties and printability. As a result, a filament should be selected correspondingly.

The steel alloy used to produce specimens in the thesis is austenitic AISI 316L. The chemical composition for AISI 316L is shown in Table 2 and the typical mechanical properties are shown in Table 3.

Table 2: The chemical composition for AISI 316L [15]. All values are given in wt%.

Fe	**C**	**Cr**	**Ni**	**Mo**	**Mn**
65	0.03	17	12	2.5	2.0

Table 3: Typical mechanical properties for hot-finished and annealed AISI 316L [15].

Property	**Symbol**	**Value**	**Unit**
Elastic modulus	E	193	GPa
Yield strength	σ_{y}	205	MPa
Ultimate tensile strength	σ_{UTS}	515	MPa
Total elongation at fracture	$\varepsilon_{\mathrm{tot}}$	0.4	-

2.2 Printing procedure

Durgun and Ertan [11] tested and examined the advantages and cons of FDM printing, as previously described. However, they indicate that the raster angle and orientation significantly impact the specimen's mechanical characteristics and production cost. The raster angle is defined as the angle formed between the nozzle direction and the bed's established x-axis [16], while the orientation is the build positioning. For maximum strength, the raster angle is generally adjusted at -45°/+45°, as shown in Figure 2. A 'dogbone'-shaped specimen is built with three possible orientations in their article: horizontal, vertical, and perpendicular. The orientation is found to have a more significant impact on mechanical characteristics and surface roughness than the raster angle.

Furthermore, there is a strong correlation between mechanical characteristics and surface roughness. Specifically, increased tensile and flexural strength with reduced surface roughness. The perpendicular orientation is not recommended due to the weak bonding between the strands. That is because the strands are built perpendicular to the applied stress. As a result, weak strand-to-strand connections are broken apart. On the other hand, a low raster angle is ideal since strands are deposited along the stress direction, giving improved results. However, if the printed specimen is expected to withstand loading in multiple directions, a combination of raster angles is optimal, such as -45°/+45°. Finally, according to Durgun and Ertan, the best design is a horizontal orientation with a 0° raster angle for the best mechanical properties, surface roughness, lowest material cost, and manufacturing time. Other research, however, reveals that vertically constructing the sintered specimen improves its properties [17]. However, it is concluded that it is extremely reliant on geometry.

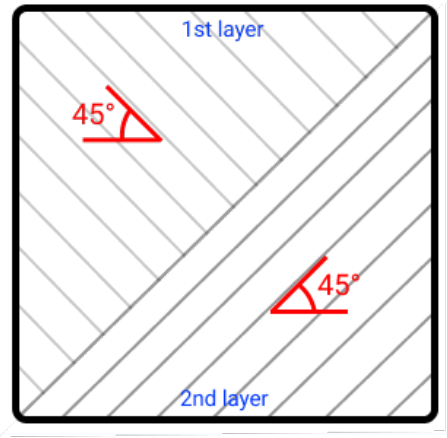

Figure 2: Top view of a specimen cross-sectionally with a -45°/+45° raster angle configuration.

The names of the different build orientations proposed by Suwanpreecha et al. [18] are vertical, side, and flat layouts. These names are used in the thesis frequently when discussing the printing orientations of specimens. The orientations are displayed in Figure 3.

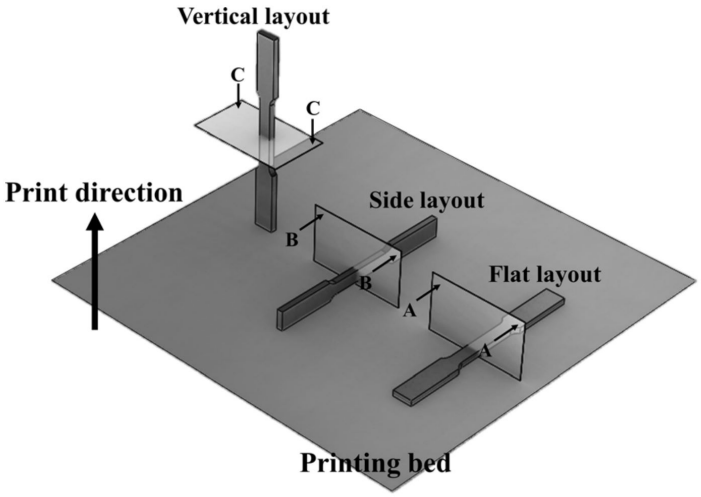

Figure 3: The three build orientations of printing a specimen suggested by Suwanpreecha et al. [18].

The metal particle size is another factor that can influence the specimen's characteristics. Fine powders are preferred in FDM, according to Masood, and Song [19] since larger particles have a higher risk of clogging the nozzle. A wider nozzle diameter can help prevent clogging. However, a specimen with thin layers and minimal surface roughness requires a smaller diameter. Because of the enhanced mobility

between the particles, the viscosity is also lowered by reducing the particle size. As a result, flowability and printability improve. In addition, to create a dense metal specimen after post-processing, the binder to powder ratio should be adjusted. It is easier to achieve suitable printing viscosity with a high binder to powder ratio, but at the cost of increased porosity during post-processing. If the ratio is reduced, optimal viscosity will be more challenging to attain, but the specimen will be denser. As a result, the filament composition must be considered while printing with FDM.

Pazhamannil et al. [20] conclude that the mechanical properties of a metal printed specimen depend on a few criteria and metal particle size. They discuss the specimen's ultimate tensile strength and how it changes as the parameters are modified. The first parameter is layer thickness, where decreasing layer thickness equals increased tensile strength. The reason is the presence of micro-voids between larger strands, which causes poor layer bonding. The second parameter is higher nozzle temperature, which enhances tensile strength and neck development rate by increasing intermolecular diffusion over the surface. Increased flow rate improves tensile strength by increasing material deposition, resulting in more compact specimens and more strands overlapping. As a result, the number of micro-voids is reduced. The flow rate is the most critical parameter to change to increase tensile strength, according to Godec et al. [21]. Some variables, such as infill speed, have little impact on tensile strength. Therefore, the speed can be raised to save production time while preserving strength.

A scientific study on manufacturing a metal specimen with FDM and post-processing was written by Liu et al. [14]. Their goal was to create a less expensive and more convenient technique for printing metals than SLS and MIM. They propose employing FDM with a metal/polymer composite filament and post-processing treatment to produce metal parts. When the filament enters the heating chamber, the polymer transforms into a semi-liquid condition, allowing for printing. The polymer distributes the metal particles equally as a result. The green part goes through debinding to remove the polymer binder and sintering to initiate grain growth and improve density after printing. Liu et al. conclude that with this technology, they can make metal specimens with mechanical properties comparable to more expensive options while staying cost-effective and efficient.

2.3 Post-processing

The specimen must be post-processed after printing in order to improve its mechanical and general qualities. The multi-component specimen's characteristics are relatively poor after production, and it is not yet suitable for high-stress applications. Post-processing is not required for pure PLA samples, but it is required to create metal specimens with high strength. This thesis removes the binder to create a pure metal specimen with an exclusively metallic character, AISI 316L, allowing the metallic particles to bond together during subsequent treatments. Three types of debinding processes are detailed in the study by Nurhudan et al. [10]: thermal, solvent, and catalytic debinding. Thermal debinding involves heating the specimen to temperatures ranging from 60°C to 600°C, depending on the binder used. The specimen is then kept at the specified temperature for a set time to allow the binder to degrade.

Furthermore, the temperature should not be too high since it can cause the binder to decompose into carbon. Heptane or trichloroethane can be used in the solvent debinding procedure. In contrast, nitric or oxalic acid can be utilized in the catalytic debinding process with a temperature range of 110°C to 150°C. The processes change only in how they are performed, but the outcomes are generally the same. Solvent debinding to remove the primary material in the binder system and thermal debinding to remove the backbone are conventional debinding procedures. Thompson et al. [13] recommend the following temperature schedule for a cylindrical AISI 316L specimen of 20mm diameter and 6mm thickness: 374°C to 750°C within a vacuum furnace (10^{-3}mbar to 10^{-5}mbar) for 1.5 hours. The specimen is now binder-free.

Multiple voids occur in the specimens after debinding, rendering them porous and producing poor mechanical properties. By causing grain growth, sintering densifies the specimen and eliminates internal porosity. Following debinding, the specimen is put to a new temperature program at higher temperatures for more extended periods. Using the same specimen as Thompson et al. [13], a suitable sintering program would be two hours at 1360°C in a vacuum environment at 10^{-3}mbar. During the sintering of a metal specimen, six driving forces occur, according to Banerjee and Joens [22]. These are condensation diffusion, surface diffusion, lattice diffusion from the surface, lattice diffusion from grain boundary, grain boundary diffusion, and plastic flow. It is important to note that not all of these parameters contribute to the specimen's densification.

Condensation diffusion, surface diffusion, and lattice diffusion from the surface all promote pore growth, which increases the porosity of the specimen. However, grain boundary diffusion, lattice diffusion from the grain boundary, and plastic flow help to eliminate pores. As a result, the material becomes denser. Surface diffusion, lattice diffusion from the surface, and condensation diffusion are all dependent on the grain size of the microstructure. The grains should be as fine as possible to facilitate the densification of the material. Temperature, diffusion coefficients, grain boundary thickness, and pore size are other factors to consider. The theoretical density of the specimens has increased to ∼99% after sintering, indicating that the specimen is no longer porous but dense. As a result of the densification, the specimen has shrunk slightly, but its mechanical properties have improved. To control shrinkage, the size of the specimen should be monitored both before and during sintering. Figure 4 illustrates the debinding and sintering operations.

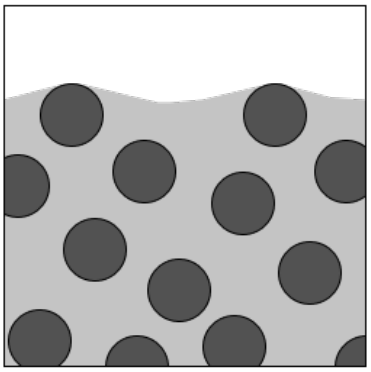

(a) Stage 1 - Original material of dispersed steel particles in a polymer matrix.

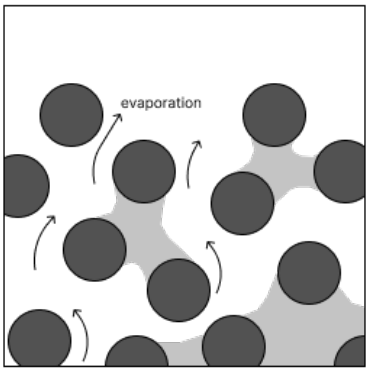

(b) Stage 2 - During debinding, the polymer exits the material by evaporation.

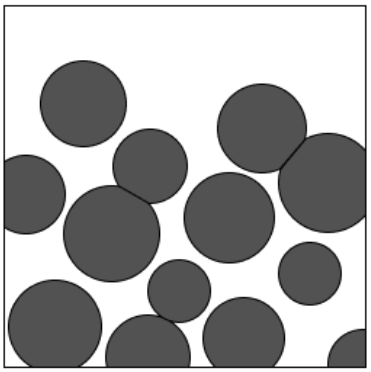

(c) Stage 3 - During sintering, grains start growing in order to eliminate pores.

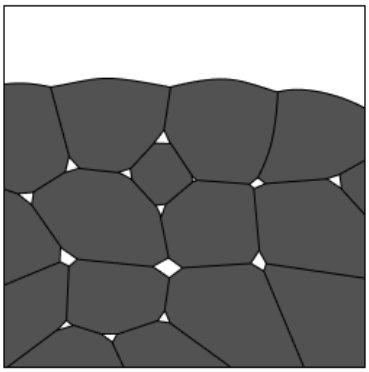

(d) Stage 4 - The material is now ~99% dense steel with some small pores at grain boundaries.

Figure 4: An illustration of the four stages of debinding and sintering at a microscopical level.

The Particle Size Distribution (PSD) of the metal powder is another crucial parameter to consider during sintering. The PSD is the difference in size between the powder's biggest and smallest particles. A high PSD indicates a wide range of particle sizes, whereas a low PSD indicates a tight size distribution. Sintering a powder with a narrow PSD has a reduced initial sintering rate but results in denser material when grain development is commenced, according to Ting, and Lin [23]. Particles have a better packing with a higher PSD. However, tiny particles are absorbed by larger particles during sintering, resulting in lower densification during grain development. As a result, powder with a low PSD is chosen.

Although the FDM specimens in this thesis are made of AISI 316L, various materials can be used in other applications. PLA can be used to print circuit boards, with silver and gold printed on top as circuits, according to Bourell et al. [24]. Making electronics using these materials is popular since PLA is non-conductive and silver/-gold is conductive. Furthermore, particular printing techniques enable exceptional precision and accuracy, building complicated circuits and advanced hardware. Another example is the application of titanium in medicine. Titanium can be utilized to produce prostheses and surgical implants because of its excellent bio and mechanical qualities. Composites can also be utilized as a feedstock in AM. For example, onyx, a composite of nylon and carbon fibers, may produce specimens with great strength, heat resistance, and chemical resistance and is utilized in engine parts.

2.4 Mechanical testing

The tensile specimen is loaded in its length direction during uniaxial tensile testing. When uniaxial stress is applied to metal specimens, they exhibit linear elastic behavior initially. Linear elastic behavior means that the specimens deform elastically linearly to the stress level, and if the specimen is unloaded, it will revert to its original length without plastic deformation. The linear elastic area can be used to calculate the elastic modulus, E, which is often used as a stiffness parameter for a material. When the stress level increases, the specimen leaves the linear elastic region and undergoes plastic deformation. The yield stress, σy, is the stress level at which the specimen begins to deform plastically. Experimentally, the offset yield strength, $\sigma_{y,0.2\%}$, is set to 0.2% elongation, where steels usually exhibit plastic behavior. The stress continues to rise until it reaches the ultimate tensile stress, σ_{UTS}. With additional elongation, the stress level begins to decline. The deformation of the gauge, where the cross-section area continuously decreases as the material is forced apart, is referred to as necking, and it is the main cause of the stress decrease. Necking is more noticeable in ductile materials, whereas brittle materials have little to no yielding or necking tendency. Finally, the total elongation to fracture, ε_{tot}, is obtained at the specimen's fracture point. A stress-strain diagram [25], in which the stress-strain relationship is graphically displayed (Figure 5), is a typical way of examining the tensile properties of a specimen.

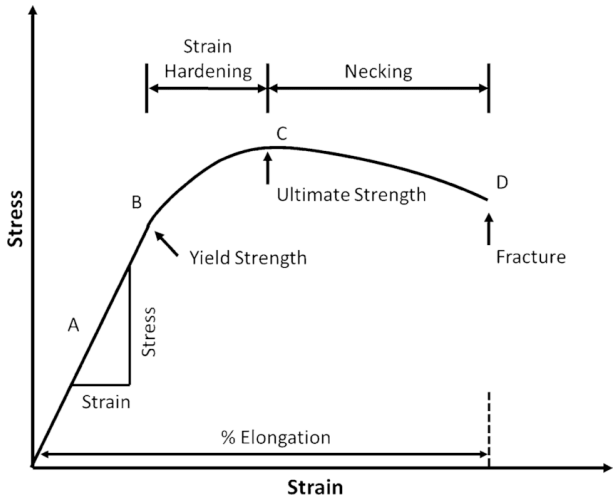

Figure 5: The stress-strain curve with the relevant information [26].

Extensometers, strain gauges, and DIC (Digital Image Correlation) can all be used to measure the specimen's elongation in practice. The gauge's elongation is measured with the extensometer. The measurement is performed by setting a reference length of the device and calculating the elongation during loading. The strain gauge, on the other hand, is an electrical instrument that detects electrical resistance fluctuations as a material deforms and translates the fluctuations into strain measurements [27]. DIC is an imaging technique that provides information on the strain, stress levels, and deformation localization. The method is usually performed by applying markings on the specimens that a camera may easily detect. The movements of the markers are subsequently detected and measured by software, which then turns the measurements into data [28]. The capacity to obtain high-quality data on material deformation at cheap costs benefits from employing DIC. It can even be used on larger structures such as bridges and buildings, as long as the program can recognize markings on the structures and compare different phases of deformation. Thus, DIC is utilized for its ability to precisely locate high-stress locations inside a material and anticipate future crack initiation and propagation sites [29].

Azadi et al. [30] discuss the mechanical properties of specimens produced with FDM under fatigue loadings. Specimens constructed with PLA and ABS are subjected to various fatigue loadings and observed in SEM to locate the crack nucleation sites and the crack propagation. Using the Basquin equation (Equation 2.1), the fatigue properties are calculated for each specimen.

$$\sigma_a = \sigma'_f (2N_f)^b \tag{2.1}$$

σ_a	=	stress amplitude
σ'_f	=	fatigue strength coefficient
N_f	=	number of cycles to failure
b	=	fatigue strength exponent

By viewing the specimens cross-sectionally in SEM, they observed that cracks initiate from dislocations in the microstructure, such as pores, contamination, and irregularities. The geometry of the pores plays a significant role in the crack initiation, where spherical pores can withstand more stress before crack initiation than a slit-shaped pore. The reason is that there is a higher stress concentration around the corners of a slit-shaped pore compared to a spherical pore without any pronounced corners [31]. Azadi et al. differentiate between pores caused by physical gaps between strands and pores caused by entrapped gas due to the material's melting during FDM. In addition to acting as stress risers, the pores contribute to reduced density and strength of the specimens. After crack initiation, striations were observed in SEM and used to measure the crack propagation and the number of cycles in Stage 2 (Figure 6). Finally, fracture surfaces were observed, which signifies the end of crack propagation and failure of the specimen (Stage 3).

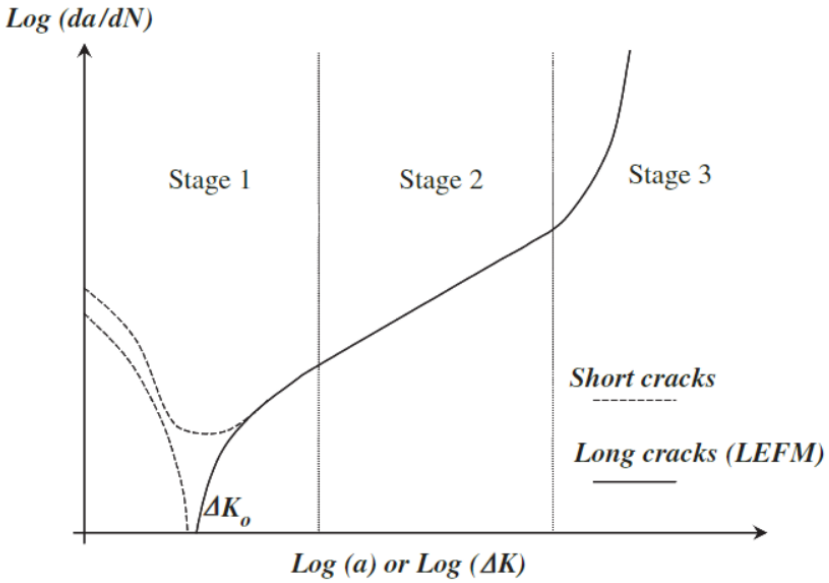

Figure 6: The rate of crack growth over the range of stress intensity. Stage 1 represents the rapid crack growth during crack initiation, steady crack propagation following the Paris' equation in Stage 2 (Equation 2.2), and rapid crack growth leading to failure in Stage 3 [32].

$$\frac{da}{dN} = C(\Delta K)^m \tag{2.2}$$

$\frac{da}{dN}$	=	fatigue crack growth per load cycle
a	=	crack length
N	=	number of load cycles
ΔK	=	stress intensity factor range
m	=	material constant

The mean stress, which is the mean value between the maximum and minimum stress of a cycle, can have a detrimental effect on the fatigue life of a specimen. Increased positive mean stress suggests that the specimen is under constant tension, while negative mean stress corresponds to compression. Steel specimens tend to have improved behavior under compression, increasing fatigue life. However, constant tension will cause earlier crack development and shorter fatigue life. When the mean stress is set to not equal zero, alterations to the original Basquin equation (Equation 2.1) are introduced to predict the fatigue life of a specimen. Since the Basquin equation does not consider the mean stress, it is necessary to use the Goodman, SWT, Walker, or Morrow methods [33]. In order to introduce the mean stress

to the Basquin equation, a new stress amplitude is introduced, σ_{ar}, where r indicates that $\sigma_m = 0$. Goodman, SWT, Walker, and Morrow use different equations to obtain σ_{ar} with a certain precision. σ_a in the Basquin equation is then replaced by σ_{ar} to accommodate σ_m. The Morrow equation (Equation 2.3) is widely used for steel specimens due to its high precision and accuracy to the real stress values in order to predict the fatigue lives (Equation 2.4).

$$\sigma_{ar} = \frac{\sigma_a}{1 - \frac{\sigma_m}{\sigma'_f}} \tag{2.3}$$

$$N_f = \frac{1}{2}\left(\frac{\sigma_a}{\sigma'_f - \sigma_m}\right)^{\frac{1}{b}} \tag{2.4}$$

According to Stephens et al. [34], the fatigue life of a steel specimen is also affected by parameters such as microstructure, geometry, surface finish, and frequency. As explained previously, the impurities, pores, and other defects in the microstructure play an essential part in determining the fatigue life of a component. Chemistry, cold working, and heat treatment may significantly influence the ultimate tensile strength of the material, which in turn affect the fatigue limit. The fatigue limit, sometimes called the endurance limit, is defined as the maximum stress level at which specimens can withstand a nearly infinite amount of load cycles without fracturing, see Figure 7. It is a valuable tool to observe which stress levels are regarded as safe and which levels where the fracture is predicted. Another factor within the microstructure is the grain size. Fine grains provide more grain boundaries, which are helpful in order to stop cracks from propagating across grains, also called crack arrest. Coarse grains result in longer distances where cracks may propagate before hitting a grain boundary, and thus fracture may occur earlier. Therefore, fine grains dramatically improve the fatigue properties of the specimen.

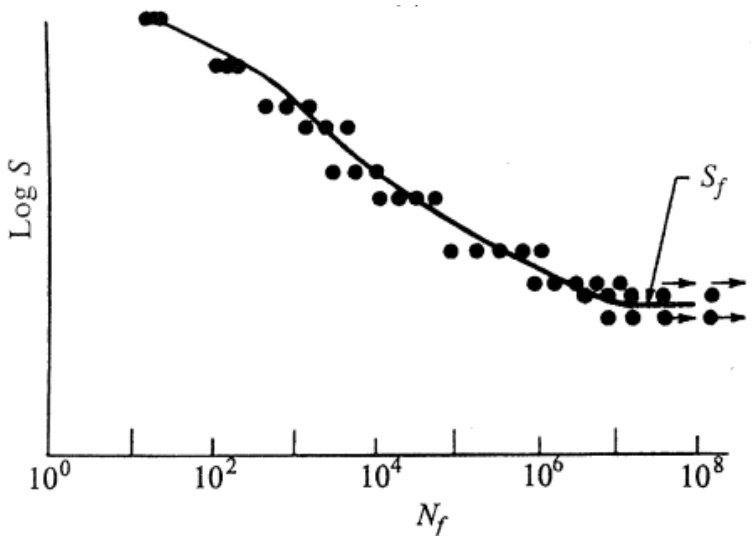

Figure 7: A typical S-N diagram where S is the stress level, and N_f is the number of cycles to failure. It is observed that the curve flattens when exceeding 10^7 cycles, which suggests that this stress level is the fatigue limit [34].

As for the specimen's geometry, a diameter or thickness of <10mm indicates that the S-N fatigue behavior is relatively independent of the geometry. However, the fatigue resistance tends to decrease when increasing the dimensions, but the results may vary depending on the testing procedure. For instance, axial versus rotational loading gives different trends in terms of fatigue behavior. Also, the loading frequency may affect the fatigue properties to a certain degree. Frequencies from 1Hz to 200Hz have a negligible effect on the fatigue properties of most metals, but abnormalities may occur when exceeding 200Hz. Hence, some effects at this frequency are usually neglected in fatigue testing. At greater frequencies, 1kHz to 25kHz, a temperature increase is often observed as the material is loaded, increasing the crack growth resistance. However, despite the advantages of the higher frequencies, it is difficult to monitor and generalize due to the high number of variables involved in the procedure.

At long fatigue lives, the effect of surface roughness becomes more pronounced. Most cracks initiate at the surface where roughness is prevalent. Thus, the optimal solution is to minimize the roughness by polishing the specimens. However, most specimens are ground or machined, which may cause slight surface degradation and reduced ultimate tensile strength. When calculating the tensile strength according to the surface conditions, a surface factor, k_f, is utilized. The surface factor is multiplied by the tensile strength, which means a lower surface factor equals decreased tensile strength. When grinding or machining a specimen, the surface factor usually ranges from 0.9 to 0.7. The surface factor is primarily due to residual stresses

emerging in the material during the surface treatment. If hot-rolled or as-forged, the surface factor may decrease further from 0.8 to 0.5, significantly affecting the tensile strength. The detrimental effect of these treatments is due to changes in the microstructure and the chemical composition. In conclusion, hot-rolled and as-forged surface conditions should be avoided for fatigue specimens to achieve long fatigue lives.

2.5 Printing terminology

Several expressions are used in the thesis when discussing the printing methods and printing parameters. The printing parameters used in the thesis are explained below with their conventional values to understand the meaning of the expressions better. Also, note that different printing software may use different terminology. In the thesis, the Ultimaker Cura software was used, which may contain different expressions than, for instance, PrusaSlicer.

Nozzle temperature is the temperature of the nozzle during printing. Different materials depend on certain nozzle temperatures to achieve excellent flowability and extrusion. For instance, printing with BASF 316L Ultrafuse requires higher temperatures than printing with PLA due to melting temperature differences. For a conventional FDM printer, the nozzle temperature is generally set in the range of 180-295°C.

Bed temperature is the temperature of the building platform, also called the bed. A higher bed temperature is necessary to minimize the temperature difference between the material and the bed so that the specimen sticks to the platform. For a conventional FDM printer, the bed temperature is generally set in the range of 80-120°C.

Infill printing speed is the speed of the extruder when printing the infill of a specimen. The infill printing speed can be adjusted to fit the desired infill quality, where slower speeds equal precise printing but at the cost of time. For a conventional FDM printer, the infill printing speed is generally set in the range of 30-60mm/s.

Wall printing speed is the speed of the extruder when printing the walls of a specimen. The wall printing speed can be adjusted to fit the desired wall quality, where slower speeds equal precise printing but at the cost of time. For a conventional FDM printer, the wall printing speed is generally set in the range of 15-30mm/s.

Initial layer printing speed is the speed of the extruder when printing the first layer of a specimen. The initial layer printing speed should be lower than the infill speed to obtain an excellent foundation for the specimen. For a conventional FDM printer, the first layer printing speed is generally set in the range of 7.5-30mm/s.

Brim printing speed is the speed of the extruder when printing the brim of a specimen. The brim extends the first layer of a specimen which improves the adhesion to the bed by increasing the surface contact. The brim printing speed should be lower than the infill speed to obtain good quality and excellent adhesion properties. For a conventional FDM printer, the brim printing speed is generally set in the range of 7.5-30mm/s.

Infill layer height is the height of the strands in the infill. Increased height results in shorter printing time, but at the cost of larger strands and less precision. Decreased height results in more precision and less visible strands, but at the cost of time. For a conventional FDM printer, the infill layer height is generally set in the range of 0.05-0.2mm

Initial layer height is the height of the strands in the first layer. The initial layer height should be higher than the infill layer height to ensure a proper foundation for the specimen. For a conventional FDM printer, the initial layer height is generally set in the range of 0.1-0.2mm

Wall/top/bottom thickness corresponds to the number of wall/top/bottom layers on the specimen. Increased thickness equals more layers, while decreased reduces the number of layers. The wall/top/bottom layers usually improve the strength of the specimen but may require more printing time. For a conventional FDM printer, the wall/top/bottom thickness is generally set in the range of 0.8-1.2mm.

Infill density is the amount of material in the infill. For most filaments, it is possible to obtain low printing time and acceptable mechanical with a decreased infill density. However, using the BASF 316L Ultrafuse filament for mechanical testing requires significantly higher density to minimize porosity and to obtain a $\sim$100% dense material after debinding and sintering. For a conventional FDM printer, the infill density is generally set in the range of 50-100%, heavily depending on the sought mechanical properties.

Infill pattern is the printing technique for the infill of a specimen. The infill pattern can be separated into several types, including lines, zig-zag, and grid (Figure 8). The pattern is selected according to the wanted density and production time, where different patterns give different results. The line pattern is typically chosen for dense specimens, while the grid is utilized when mechanical properties are less significant to decrease production time.

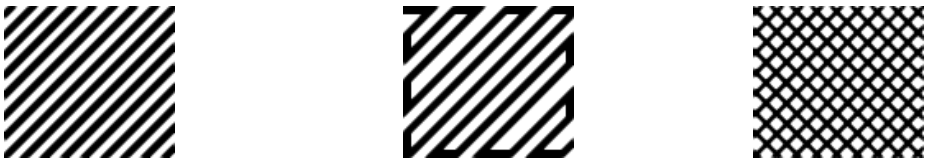

(a) Lines **(b)** Zig-zag **(c)** Grid

Figure 8: Three infill pattern alternatives.

Infill overlap percentage is how much the infill overlaps the inner walls (Figure 9). Increased overlap may ensure that the infill and the walls are appropriately connected, while decreased overlap can lead to gaps between the infill and the walls. However, too much overlap may create uneven surfaces and deformations. For a conventional FDM printer, the infill overlap percentage is generally set to 5-30%.

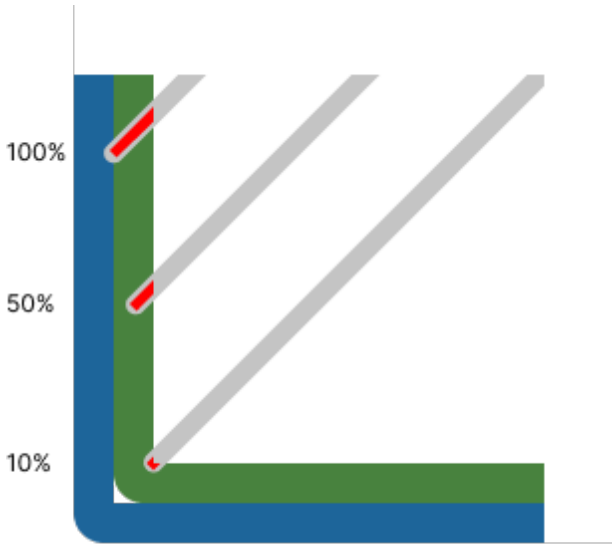

Figure 9: The overlap (red) shows how much of the infill is overlapping the inner wall (green). When the infill reaches the outer wall (blue). The overlap percentage is 100%.

Skin overlap percentage is how much the infill of the bottom/top layer overlaps the inner walls. The infill, in this case, is not the infill of the specimen but rather

the middle section of just the top/bottom layer. Like the infill overlap percentage, an increased skin overlap percentage may give the best results regarding density and decreased deformation. For a conventional FDM printer, the skin overlap percentage is generally set to 5-30%.

Infill cooling fan percentage is the intensity of the cooling fan during the infill printing. Increased cooling fan percentage causes the extruded material to cool down faster than decreased cooling fan percentage. For a conventional FDM printer, the infill cooling fan percentage is generally set to 0-100%.

Initial cooling fan percentage is the intensity of the cooling fan during the printing of the initial layer. Similar to the infill cooling fan percentage, increasing the initial cooling fan percentage causes the extruded material to cool down faster than decreased cooling fan percentage, which encourages more material flow. Decreased initial cooling fan percentage may be beneficial for the first layer to melt the strands together and act as a great foundation. For a conventional FDM printer, the initial cooling fan percentage is generally set to 0-100%.

Infill flow rate multiplier controls the amount of material extruded during infill printing. Increasing the multiplier increases the amount of material while decreasing the multiplier decreases the amount of material. Increasing the multiplier may be beneficial to ensure proper filling of pores but can lead to deformation if too much is extruded. For a conventional FDM printer, the infill flow rate multiplier is generally set to 90-110%.

Initial flow rate multiplier controls the amount of material extruded during the printing of the initial layer. Increasing the multiplier increases the material deposition while decreasing the multiplier decreases deposition. Increasing the multiplier may be beneficial for the initial layer to ensure a proper foundation, but too much material should be avoided to decrease deformation. A conventional FDM printer's initial flow rate multiplier is generally set to 90-110%.

3 Material and methods

3.1 Apparatus and material

3.1.1 Filament - BASF 316L Ultrafuse

The printing filament is a metal-polymer composite material, consisting of >80wt% austenitic AISI 316L powder and <20wt% polymer binder [35]. The filament is non-hygroscopic, which means that the material does not absorb water or humidity that may harm the steel particles [36]. The advantages of using this filament is the low cost, enabling metal printing with conventional FDM printer, and being easily applicable for FFF [37]. The specifications for BASF 316L Ultrafuse is given in Tables 4, 5 and 6.

Table 4: The preliminary specifications for BASF 316L Ultrafuse [35].

Preliminary filament specifications		
Property	**Typical value (Ø 1.75mm)**	**Unit**
Metal load	>80	wt%
Filament diameter	±50	µm
Roundness	±50	µm
Density	5	g/cm^3
Length per spool	250	m (approx.)
Weight per spool	3	kg (approx.)

Table 5: The theoretical material properties of BASF 316L Ultrafuse for CAD simulations after debinding [38].

Material properties for CAD simulations.		
Property	**Typical value**	**Unit**
Young's modulus	210	GPa
Poisson's ratio	0.4	-
Density	4700	kg/m^3

Table 6: The recommended printing parameters for BASF 316L Ultrafuse [35].

Property	Typical value	Unit
Extruder temperature	235	°C
Build platform temperature	90	°C
Nozzle diameter	0.4	mm
Infill printing speed	30	mm/s
Layer height	0.15-0.2	mm

3.1.2 Design software - SOLIDWORKS®

SOLIDWORKS® is used to design the specimens with the correct dimensions for future printing. The designed drawings are converted into STL files for Ultimaker Cura.

3.1.3 Printing software - Ultimaker Cura 4.11.0

The version of Ultimaker Cura that was used for the thesis was 4.11.0. This software is utilized to adjust printing parameters and preview a specimen before printing. STL files exported from design software are imported to Ultimaker Cura to adjust the printing parameters. G-codes of the final specimen are then exported from the software and used for printing.

3.1.4 Printer - Prusa i3 MK3

The printer used in the thesis is the Prusa i3 MK3 (Figure 10). Its main components are the extruder, cooling fans, and the build plate. The printer is capable of printing in three dimensions by altering the height of the build plate and the position of the extruder. It has a precision of 0.1mm on the z-axis and 0.3mm on the x and y-axis. However, these can be reduced to 0.05mm if calibrated before use. It is also specified that the precision also depends on the material, printing parameters, and overhangs [39]. For the thesis, a 0.4mm hardened steel nozzle is used to print the metal specimens. Due to the solid steel particles in the filament, printing with a regular brass nozzle can potentially wear out the nozzle.

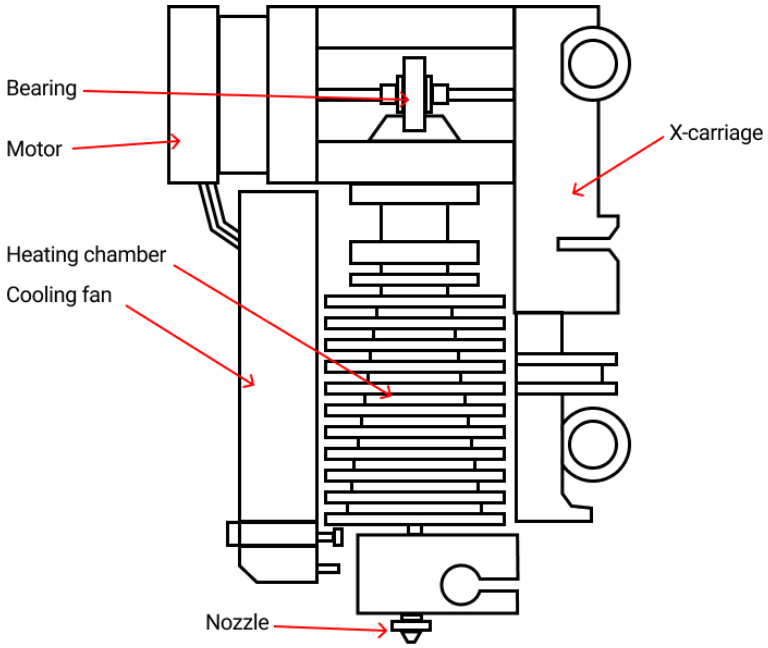

Figure 10: The main components of the Prusa i3 MK3 extruder redrawn from 3D model [40].

3.1.5 Printing glue - Magigoo 3D printing adhesive Ultrafuse 316L

The Magigoo 3D printing adhesive Ultrafuse 316L is a dedicated printing glue for the filament used in the thesis. It improves adhesion between the specimen and the build plate during printing to prevent warping. This glue is usually necessary when printing larger specimens, while for small specimens constructing a brim is sufficient.

3.1.6 Weight - Mettler Toledo AG204 DeltaRange®

The Mettler Toledo AG204 DeltaRange® is used to weigh the specimens for future calculations. This weight is chosen due to its high precision. It has readability of 0.1mg and a long-term drift sensitivity of ±0.003%. The weight is in a closed environment, which contributes to the high precision [41].

3.1.7 Fatigue testing - Instron®-ElectroPuls®-E10000

For uniaxial fatigue testing, the Instron-ElectroPuls-E10000 is used. The apparatus is equipped with replaceable grippers, suitable for fatigue, tensile, and fracture testing. The apparatus is controlled by computer software which regulates factors such as stress amplitudes, mean stresses, and a maximum number of cycles. Differ-

ent loading profiles may be selected in the software so that tensile testing may be performed using solely uniaxial elongation. The maximum load is limited to 10kN.

3.1.8 Tensile testing - Instron®-8854 Axial-Torsion System-250 KN

For uniaxial tensile testing, the Instron®-8854 Axial-Torsion System-250 KN is used. It is equipped with two grippers that grip the specimen automatically depending on a set grip pressure. Two rulers are installed on the top and bottom gripper to make it easier to place the specimen vertically before loading. The maximum load of the machine is 250kN, and it supports both uniaxial loading and torsion.

3.1.9 DIC - Digital Image Correlated - Vic-2D-v6

A camera setup is used during tensile testing to capture the elongation of the specimen. The procedure is performed using a camera connected to a computer that captures images during the tensile loading. A spotlight is set up near the camera, pointing at the specimen for improved image quality. For post-processing of the images, the Vic-2D-v6 software is used.

3.1.10 Fractography - FEI Quanta FEG 650 SEM

The FEI Quanta FEG SEM is used to perform fractography of the tensile and fatigue specimens after mechanical testing. It is an excellent technique to observe and analyze the origin and severity of crack development within a material. In addition, other defects such as pores and impurities are easily observed using SEM, which gives the user information about the microstructure and its implications on the mechanical properties. The microscope is equipped with a vacuum chamber and sensors for the secondary electron (SE) and back-scattered electron imaging (BSE). It operates at 20kV and level 6 (30µm) aperture size for regular SE imaging.

3.2 Experimental procedure

The experimental procedure is divided into several steps, which are represented in Figure 11.

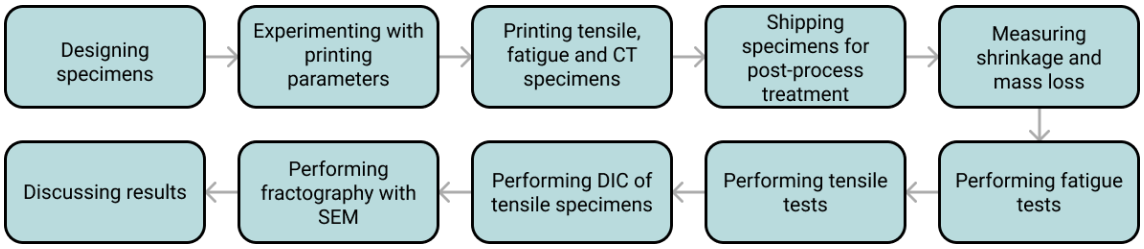

Figure 11: The main steps of the experimental procedure in the represented order.

3.2.1 Preface

Specific printing parameters are set to print green parts for post-processing and analysis. Optimal parameter configurations used for printing the specimens in the thesis were based on the optimal configurations from the specialization project by printing small specimens (Figure 12). The printing configurations from the specialization project are shown in Table 7. Due to the larger geometries of the specimens in the thesis, several additions to the printing parameters were introduced. For printing, the specimen types were tensile specimens, fatigue specimens, and CT specimens. In total, five tensile specimens and 12 fatigue specimens were printed. Three specimens were printed with a flat and side layout for the CT specimens and two with a vertical layout, totaling eight specimens. These three build orientations are represented in Figure 3. The reason for only printing two vertical CT specimens is due to weight limits for shipping, where having three vertical CT specimens exceeded the maximum allowable shipping weight.

Figure 12: Printed specimen from the specialization project with dimensions of 1cm×1cm×1cm

Table 7: These are the optimal printing configurations from the specialization project. Previously, the configurations were named after the specimens that were used to analyze the printing parameters (22, 23, 30), but for the sake of simplicity in the thesis, the configurations are named 1, 2, and 3, respectively.

Optimal printing configurations from specialization project			
Configuration	**Nozzle temperature [°C]**	**Infill printing speed [mm/s]**	**Layer height [mm]**
1	295	15	0.1
2	280	15	0.1
3	295	30	0.05

3.2.2 Precautions for designing specimens

During the sintering of the specimens, the specimens undergo densification and, as a result, shrinkage. This shrinkage has to be compensated for during the design process of the specimens. Therefore, the specimens are designed slightly larger than the original ASTM standards. Thus, the specimens are designed to be 19% longer in the x/y-direction, and 21% longer in the z-direction [35].

3.2.3 Transition from small to large specimens

In the specialization project, small solid specimens of 1cm×1×1cm were printed to observe multiple printing configurations without being too time-consuming and material expensive. The optimal configurations obtained in the project resulted in excellent print quality for small specimens. However, adhesion to the bed played a more critical role when printing larger specimens as the dimensions increased. As a result, all specimens had increased overlapping, and decreased cooling fan speed to establish a proper foundation for the initial layer. That was to ensure that the strands in the initial layer were thick enough and adequately fused to secure the foundation for the rest of the specimen.

Also, all specimens were printed with a brim to improve the adhesion between the specimen and the bed. This addition increases the surface area and decreases warping due to poor adhesion. While the brim was a great contributor to the bed adhesion, glue was also utilized. A thin layer of glue was spread evenly onto a cold bed and heated up as the bed temperature increased. As the bed was heated to the working temperature, the printing initiated.

During the first sessions of printing, the printer had to be adequately heated to produce great prints without causing a maximum temperature error. The heating was done by producing one or two test specimens before printing the actual specimens. Without this procedure, it could cause the nozzle temperature to exceed the maximum temperature of 300°C and stop the print. The travel speed was also increased from 120mm/s to 200mm/s to decrease the time spent on interlayer movement. This increase reduced the time frame where the printer was not extruding material and ensured that the nozzle temperature did not increase much. It also helped produce a more cohesive specimen without long pauses between layers.

Note that the infill printing speed is different from the wall printing speed. The wall printing speed is the printing speed of the outer walls, including the top and bottom layers, and it is precisely half of the infill printing speed. Therefore, the thesis does not explicitly mention the wall printing speed since it can easily be derived from the infill printing speed. By default, the inner wall speed is equal to the infill speed, but this was set equal to the outer wall speed for all specimens to avoid speed differences while printing the walls. The wall speed mainly affects the surface quality and roughness, while the infill speed serves a more structural purpose. Also, while these two parameters are separated, they may still affect each other if one is not optimal.

3.2.4 Designing the tensile specimen

The tensile specimens were designed in SOLIDWORKS according to ASTM E8/E8M standard test methods for tension testing of metallic materials [42]. However, due to issues related to the oversizing of the specimens to accommodate for shrinkage, the radius was reduced from 6mm to 5mm. When using a radius of 6mm, the total length of the specimen exceeded the overall length of 100mm. This could be compensated for by decreasing A or B from Figure 13, but it was decided that the radius, R, should be decreased. The dimensions of the tensile specimen is shown in Table 8, and Figure 13, 14.

Table 8: The theoretical dimensions of the tensile specimens from the ASTM standards [42], and the elongated dimensions to compensate for shrinkage after sintering are shown. All dimensions in the x/y-direction are enlarged by +19%. This includes all values except T, which is enlarged by +21% [35].

Theoretical dimensions of tensile specimen		
Dimension	**Post-sintering [mm]**	**Pre-sintering [mm]**
W	6.00	7.14
T	3.00	3.63
R	6.00	7.14
L	100.00	119.00
A	32.00	38.08
B	30.00	35.70
C	10.00	11.90

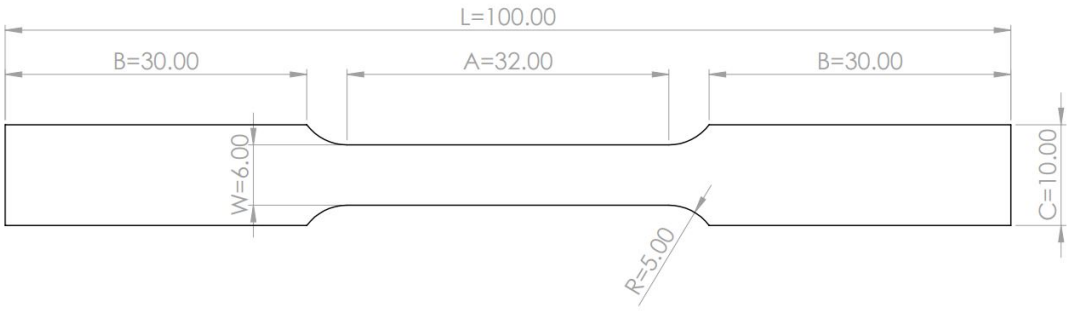

Figure 13: All dimensions are given in mm. The top surface of the tensile specimen is shown with its relevant dimensions.

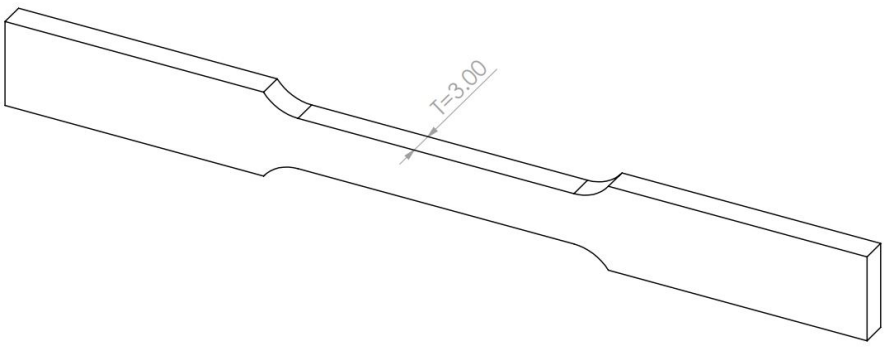

Figure 14: All dimensions are given in mm. The figure shows the thickness of the tensile specimen.

3.2.5 Designing the fatigue specimen

The fatigue specimens were designed in SOLIDWORKS according to ASTM E466-21 standards for conducting force controlled constant amplitude axial fatigue tests of metallic materials [43]. The dimensions of the fatigue specimen are shown in Table 9, and Figure 15, 16.

Table 9: The theoretical dimensions of the tensile specimens after sintering from the ASTM standards [43], and the elongated dimensions to compensate for shrinkage after sintering are shown. All dimensions in the x/y-direction are enlarged by +19%. This includes all values except T, which is enlarged by +21% [35].

Theoretical dimensions of fatigue specimen		
Dimension	**Post-sintering [mm]**	**Pre-sintering [mm]**
W	4.00	4.76
T	2.00	2.42
R	32.00	38.08
L	77.06	91.70
A	27.06	32.20
B	25.00	29.75
C	10.00	11.90

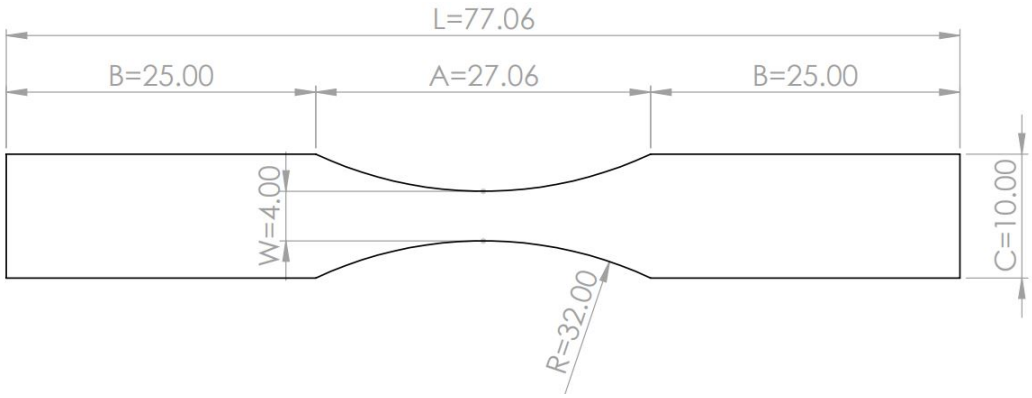

Figure 15: All dimensions are given in mm. The top surface of the fatigue specimen is shown with its theoretical dimensions after post-processing treatment.

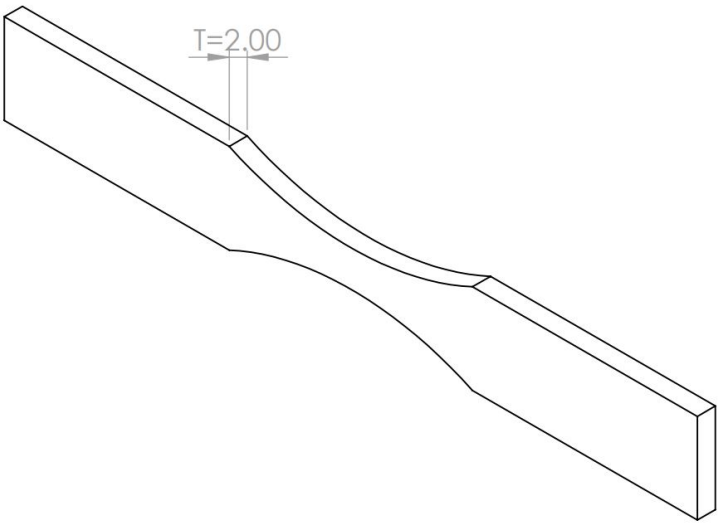

Figure 16: All dimensions are given in mm. The figure shows the thickness of the tensile specimen.

3.2.6 Designing the CT specimens

Initially, the CT specimens were designed as solid specimens without holes or a notch. These sections would be machined into the specimen after post-processing treatment, thus forming the final CT specimen geometry. However, as explained previously in Section 1.3, the machining and mechanical testing of the CT specimens were not performed due to time restrictions and technical issues with the machining tools. Thus, machining the CT specimens is explained but not performed. According to the ASTM E1820-18 standard test method for measurement of fracture toughness, [44], the dimensions of the CT specimen are dependent on the set width, W, of the specimen.

In contrast to the tensile and fatigue specimen, the width of the CT specimens is the distance from the side to the center of the holes, as shown in Figure 17. After this is set, the other dimensions are calculated as width parameters. It was decided that the specimen should be printed in three different build orientations (Figure 3) to observe how it affects the print quality. It was essential to consider the shrinkage during sintering since the x/y/z-directions change when changing the build orientation. In addition, after debinding and sintering, the specimens were designed to be machined to obtain smooth surfaces. Hence, 0.5mm was added to each side to have some extra material for machining. The dimensions for the specimens before sintering, before machining, and after machining are given in Table 10, where stages separate the dimensions:

Stage 1 - The theoretical dimensions of the specimen post-sintering and post-machining from the ASTM standards [44].

Stage 2 - The dimensions of the specimen post-sintering and pre-machining.

Stage 3 - The dimensions of the specimen pre-sintering and pre-machining.

Table 10: The theoretical dimensions of the CT specimens from the ASTM standards [44], and the elongated dimensions to compensate for shrinkage after sintering and for machining are shown. The table is separated into three groups by shading: (from top) flat layout, vertical layout, and side layout.

Theoretical dimensions of CT specimens			
Dimension	**Stage 1 [mm]**	**Stage 2 [mm]**	**Stage 3 [mm]**
T	12.00	13.00	15.73
L	30.00	31.00	36.89
H	28.80	29.80	35.46
A	5.88	-	-
W	24.00	-	-
R	6.00	-	-
T	12.00	13.00	15.47
L	30.00	31.00	36.89
H	28.80	29.80	36.06
A	5.88	-	-
W	24.00	-	-
R	6.00	-	-
T	12.00	13.00	15.47
L	30.00	31.00	37.51
H	28.80	29.80	35.46
A	5.88	-	-
W	24.00	-	-
R	6.00	-	-
	=	Flat layout	
	=	Vertical layout	
	=	Side layout	

Logically, the dimensions in Stage 3 are larger than in Stage 2 and 1 since it has to accommodate the future shrinkage of the specimen in addition to machining. Dimensions in Stage 2 are also larger than the values in Stage 1 since machining the edges has not yet been performed. Note that the radius is added after sintering and machining. Therefore it only occurs in Stage 1. The same is told for the width, W, and dimension A. These dimensions depend on the distance from the edge/height after machining to the center of the holes.

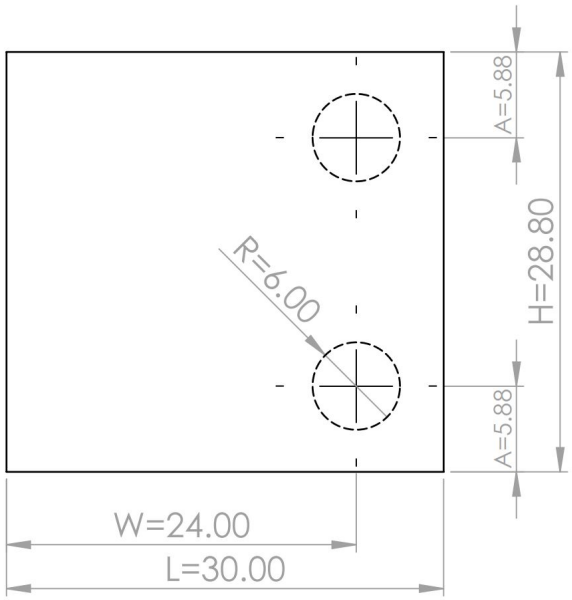

Figure 17: All dimensions are given in mm. The front of the CT specimen is shown with its theoretical dimensions after post-processing treatment. This is the specimen before machining a notch and holes. As a result, the dashed circles represent the locations of the holes which are drilled during machining.

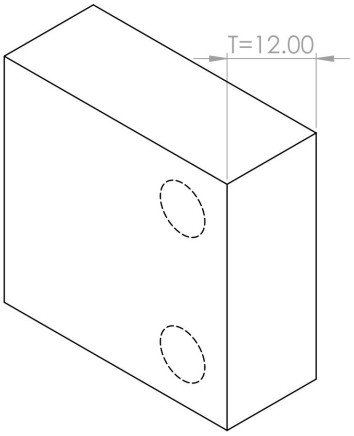

Figure 18: All dimensions are given in mm. The side of the CT specimen is shown with its theoretical dimensions after post-processing treatment. This is the specimen before machining a notch and holes. As a result, the dashed circles represent the locations of the holes which are drilled during machining.

3.2.7 Calibration of printer

In order to ensure that the material adhered correctly to the bed, the height of the nozzle had to be properly adjusted. This was done by the First Layer Calibration setting. Using this function, the printer printed long strands across the bed and finished with a small quadratic layer. By doing this, it could easily be observed if the nozzle was too close to the bed or if it was too high. In Figure 19a, gaps and deformations are observed, which is a typical result of the nozzle being set too high. On the other hand, in Figure 19c, the material is being squished due to the low placement of the nozzle. This results in poor shape of the strands, and the layers become too thin. Figure 19b shows the optimal calibration where the strands adhere nicely to the bed, and no gaps are visible.

(a) Too high **(b)** Good **(c)** Too low

Figure 19: Three first layer calibrations; **(a)** z=-0.700mm being too high, **(b)** z=-0.860mm being good, and **(c)** z=-1.050mm being too low.

In addition to the First Layer Calibration, the bed was calibrated using the Bed Level Correction. Using this calibration technique, each side of the bed was adjusted individually to compensate for an uneven printing platform. This was necessary to obtain even printing and improved uniformity. The calibration settings for the bed is shown in Table 11, and figures of the calibrated and non-calibrated specimens are shown in Figure 20. However, this is highly dependent on the printer and may not be necessary for all devices.

(a) Non-calibrated

(b) Calibrated

Figure 20: The first layer of two fatigue specimens using the non-calibrated and calibrated settings for the Bed Level Correction. **(a)** shows gaps between strands due to poor calibration, which are absent in **(b)**.

Table 11: The table shows the settings for the Bed Level Correction calibration. Negative values signify that the distance between the area and the nozzle decreases, while positive values increase the distance.

Bed Level Correction settings	
Front	-55µm
Back	5µm
Left	-40µm
Right	0µm

3.2.8 Troubleshooting during printing

It was evident from initial printing that the optimal printing configurations from the specialization project for small specimens needed to be tweaked to accommodate the

larger specimens in the thesis. Using the configurations from Table 7, many deformations, high surface roughness, high internal porosity, and warping were observed. In addition, deformations on the seam was particularly prevalent for the tensile and fatigue specimens and could potentially cause premature failure during mechanical testing.

As discussed in Section 3.2.3, preheating the nozzle, calibrating the printer, and the addition of glue, were all necessary to ensure that the specimens adhered to the bed and reduced warping. Besides, the preheating of the nozzle was worthwhile to decrease the risk of getting the maximum temperature error caused by the nozzle temperature exceeding the maximum allowed temperature set by the printer.

To decrease the surface roughness on the sides of the specimens, multiple trials were made. However, it was clear that the main parameter influencing the roughness was the cooling fan percentage. As shown in Figure 21, the surface roughness greatly decreases with decreasing percentage, where 50% (Figure 21c) gave the best results. Decreasing the percentage below 50% resulted in some undesirable traits regarding the surface quality, and it was concluded that 50% was the optimal value.

(a) 100%

(b) 75%

(c) 50%

Figure 21: Three fatigue specimens printed with three cooling fan percentages. Surface roughness decreases with decreasing cooling fan percentage.

Since the specimens were printed onto the bed with glue to increase adhesion, special precautions were taken for the specimen removal. When removing the specimens directly from the bed immediately after printing, tearing and breakage were normal. The build plates with the specimens were submerged to prevent the defects. A bucket with hot water was used to dissolve the glue and loosen the specimen. It is important to note that the glue was water-soluble, which was a requirement for this procedure. The plates were usually submerged in water for up to 12 hours so that the specimens loosened without using special removal equipment.

Initially, when printing the first layer with 0.1mm, the layer became stringy without strands merging. The lack of merging was solved by increasing the initial layer height to 0.2mm. Also, to ensure that the strands merged into one uniform layer, the overlapping percentage was increased, and the initial printing speed was decreased.

A section that proved to be troublesome during printing was the seam. There were excessive deformations at the seam and the wall following it. The deformations would have significant implications, especially on the fatigue specimens, since the seam was near the gauge and could act as a crack initiation site if not improved. The seam was then manually relocated to the sharpest corner on the backside of the specimen in Ultimaker Cura. When printing the walls of each specimen, the printer permanently moved counterclockwise to the specimen (Figure 22). The seam was relocated to the back right corner so that the possible site for deformations following the seam was the smallest. In addition, the increased deformation is located in the gripping area, which is of no interest during mechanical testing. This, along with the inner/outer wall speeds explained in 3.2.3, resulted in much nicer seams and drastically improved surface quality, as seen in Figure 23.

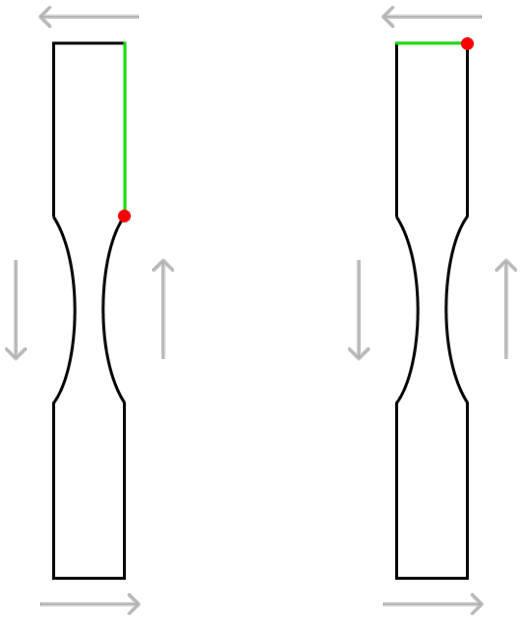

(a) Before **(b)** After

Figure 22: Two fatigue specimens are shown before and after the relocation of the seam. The red dots represent the seams, the green sides represent the walls following the seam with increased deformation, and the gray arrows represent the wall printing directions.

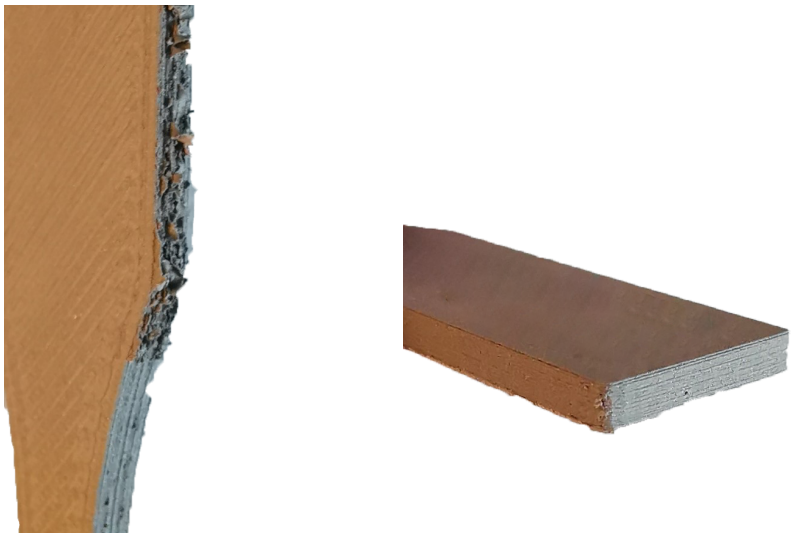

(a) Before **(b)** After

Figure 23: The figures show the placement of the seam, and the following deformations.

According to the optimal printing configurations from Table 7, the optimal layer height was sought to be either 0.1mm or 0.05mm. For the small specimens in the

specialization project, the 0.05m layer height resulted in the best surface quality. However, for the specimens in the thesis, some deformation, misalignment and rupture of strands were observed during the infill printing, and especially in the gauge. These defects were not present when using the 0.1mm layer height, and thus the printing procedure was continued using 0.1mm instead of 0.05mm.

3.2.9 Mechanical testing

Fatigue testing was performed using the Instron®-ElectroPuls®-E10000 with uniaxial load cycles. 10 fatigue specimens are used for fatigue testing to estimate the fatigue behavior of the specimens. These properties include the Basquin constants using Equation 2.1, such as the fatigue strength coefficient, σ'_f, and the fatigue strength exponent, b. Based on the theoretical fatigue values of conventional AISI 316L, it was assumed that the printed fatigue specimens would have worse performance. Thus, the selected stress amplitudes used for testing were in the range of 80MPa to 300MPa, even though conventional AISI 316L may operate in 290MPa to 380MPa [45]. When entering the low cycle fatigue (LCF) area ($< 10^4$ cycles to failure), the Basquin equation is not applicable. This is also true for the run-out points exceeding 2,000,000 cycles. As a result, the stress range is selected to obtain fatigue data in high cycle fatigue, HCF ($\geq 10^4$ cycles), below 2,000,000 cycles so that the Basquin equation may be used. The upper and bottom part of each specimen were gripped 1.5cm from each edge (Figure 24) and tightened manually to prevent slippage during loading. No friction pads were necessary to increase the grip, as the tightening of the grippers was sufficient. Parameters needed by the software, such as the mean stress and the conversion from stresses to loads, were calculated manually based on the stress amplitude, the stress ratio, and the measured dimensions of the specimen. For the thesis, the stress ratio was set to 0.1, meaning that $\sigma_m > 0$. Note that all fatigue tests are performed in standard state conditions.

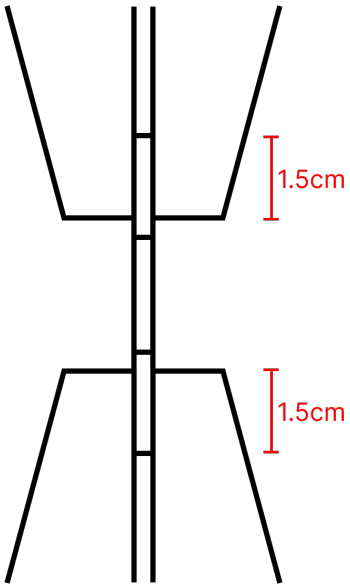

Figure 24: The upper and bottom gripper on the fatigue specimen. The specimen is gripped 1.5cm from each edge and tightened to prevent slippage. The image is not to scale, but to illustrate the set-up of the fatigue testing.

The Instron®-8854 Axial-Torsion System-250 KN was utilized for performing tensile testing of the tensile specimens. Three tensile specimens were used for testing to obtain the tensile properties. These properties include the elastic modulus, E, the offset yield strength at 0.2% elongation, $\sigma_{y,0.2\%}$, ultimate tensile strength, σ_{UTS}, and the total elongation at fracture, ε_{tot}. Initially, it was proposed to use all five specimens. However, due to some technical issues when performing tensile tests with the Instron®-ElectroPuls®-E10000, two specimens were destroyed before acquiring sufficient data. Thus, the procedure proceeded with three specimens. Similar to Figure 24, the tensile specimens were gripped between an upper and bottom gripper, which were controlled remotely, and the specimens were clamped 2cm from each edge. The strength of the grippers was dependent on a set grip pressure, which was set to 30bar for the tensile specimens. Increasing the grip pressure resulted in deep indentations in the specimens, and it was theorized that the indentations could result in early fracture in the gripping area. Hence, the pressure was decreased to 30bar to obtain a good grip without harming the specimen. In the computer software, the ramp rate was set to 1mm/min, and the data capture frequency was set to 2Hz, meaning that the software captured two points of data per second. Similarly to the fatigue testing, all tensile tests were performed in standard state conditions.

The tensile tests were combined with a DIC setup to measure and localize the elongation and strain of the specimens. By applying a thin coat of white paint with black dots to the specimens, the software could measure the relations between the

dots as the specimens deformed. Thus, the software localized the maximum strain where the maximum elongation between dots was observed. These strain values were later used to calculate mechanical properties such as the elastic modulus, and the total elongation at fracture.

4 Results

25 green parts were produced by FDM and shipped for debinding and sintering. Figure 25 shows all the green parts, which include five tensile specimens, 12 fatigue specimens, three flat CT specimens, three side CT specimens, and two vertical CT specimens.

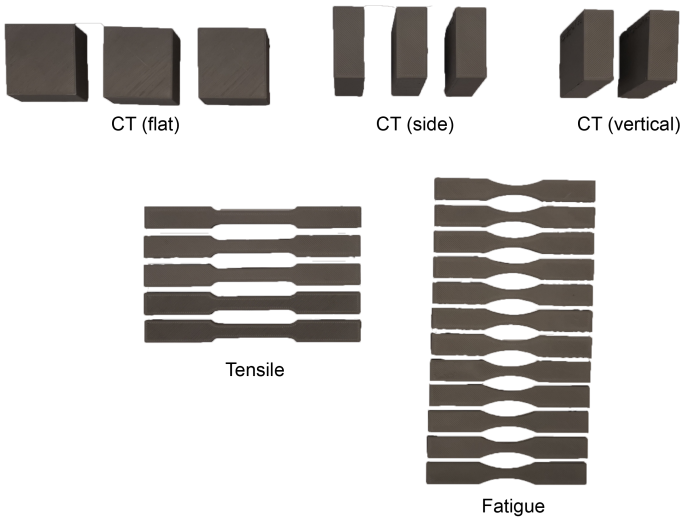

Figure 25: An overview of all specimens prior to debinding and sintering. The specimens are oriented according to their respective build orientations, where the build direction is out of the image.

4.1 Optimization of process parameters

4.1.1 Tensile and fatigue specimens

One printing configuration was utilized to print the tensile and fatigue specimens. This configuration is similar to the optimal configuration 3 from Table 7 in terms of nozzle temperature and layer height. However, several new parameters in Table 12 are introduced to print the larger specimens.

Table 12: The printing parameters for the tensile and fatigue specimens with their respective values. Parameters not stated in the table is kept at default in the printing software.

Printing parameters for tensile and fatigue specimens		
Printing parameter	**Value**	**Unit**
Nozzle temperature	295	°C
Bed temperature	100	°C
Initial printing speed	30	mm/s
Infill printing speed	30	mm/s
Wall printing speed (inner/outer)	7.5	mm/s
Initial layer height	0.2	mm
Infill layer height	0.1	mm
Initial cooling fan percentage	0	%
Infill cooling fan percentage	50	%
Skin overlap percentage	30	%
Infill overlap percentage	10	%
Initial flow rate multiplier	100	%
Infill flow rate multiplier	100	%
Number of walls	2	-
Number of top layers	1	-
Number of bottom layers	1	-

4.1.2 CT specimens

The CT specimens are printed mainly using the same printing parameters as for the tensile and fatigue specimens (Table 12). Changes are made by altering the nozzle temperature, the initial layer height, and the bed temperature.

Table 13: The printing parameters for the CT specimens with their respective values. This table is similar to Table 12 except for certain parameters highlighted in blue. Parameters not stated in the table are kept at default in the printing software.

Printing parameters for CT specimens		
Printing parameter	**Value**	**Unit**
Nozzle temperature	290	°C
Bed temperature	110	°C
Initial printing speed	30	mm/s
Infill printing speed	30	mm/s
Wall printing speed (inner/outer wall)	7.5	mm/s
Initial layer height	0.15	mm
Infill layer height	0.1	mm
Initial cooling fan percentage	0	%
Infill cooling fan percentage	50	%
Skin overlap percentage	30	%
Infill overlap percentage	10	%
Initial flow rate multiplier	100	%
Infill flow rate multiplier	100	%
Number of walls	2	-
Number of top layers	1	-
Number of bottom layers	1	-

4.2 Accuracy and surface morphology of green parts

4.2.1 Tensile specimens

Due to inaccuracies of the printer, the dimensions of the tensile specimens differ slightly from the calculated values obtained in Section 3.2.4. The average dimensions of the printed tensile specimen are shown in Table 14 with deviation to show how the theoretical and real dimensions correlate. The real dimensions are the average dimensions of the printed tensile specimens. The green tensile specimen is shown in Figure 26.

Table 14: The calculated dimensions to compensate for shrinkage after sintering, from Table 8, and the real average dimensions of the tensile specimens after printing. Not all dimensions from Table 8 are considered due to being difficult to measure.

Dimensions of green tensile specimen			
Dimension	**Calculated [mm]**	**Real [mm]**	**Deviation [mm]**
W	7.14	7.35	0.21
T	3.63	3.57	-0.06
L	119.00	118.84	-0.16
B	35.70	35.88	0.18
C	11.90	12.18	0.28

Figure 26: The green tensile specimens.

4.2.2 Fatigue specimens

Using the same argument as for the tensile specimens, the average dimensions of the fatigue specimens may differ slightly from the calculated values obtained in Section 3.2.5. These dimensions are shown in Table 15, and the specimens is shown in Figure 27.

Table 15: The calculated dimensions to compensate for shrinkage after sintering, from Table 9, and the real average dimensions of the fatigue specimens after printing. Not all dimensions from Table 9 are considered due to being difficult to measure.

Dimensions of green fatigue specimen			
Dimension	**Calculated [mm]**	**Real [mm]**	**Deviation [mm]**
W	4.76	5.07	0.31
T	2.42	2.42	0.00
L	91.70	91.67	-0.03
A	32.20	32.28	0.28
B	29.75	30.26	0.51
C	11.90	12.17	0.27

Figure 27: The green fatigue specimen.

4.2.3 CT specimens

Similar to the tensile and the fatigue specimens, the average dimensions of the flat, side, and vertical CT specimen differ slightly from the calculated values obtained in Section 3.2.6. These dimensions are shown in Table 16, and the specimens is shown in Figure 28.

Table 16: The calculated dimensions to compensate for shrinkage after sintering and machining, from Table 10, and the real average dimensions of the CT specimens after printing. The table is separated by shading: (from top) flat layout, vertical layout, and side layout. Not all dimensions from Table 10 are considered due to being irrelevant for this comparison.

Dimensions of green CT specimens			
Dimension	**Calculated [mm]**	**Real [mm]**	**Deviation [mm]**
T	15.73	15.50	0.23
L	36.89	37.13	0.24
H	35.46	35.77	0.31
T	15.47	15.71	0.24
L	36.89	36.16	-0.73
H	36.06	36.98	0.92
T	15.47	15.77	0.30
L	37.51	37.57	0.06
H	35.46	35.55	0.09
	=	Flat layout	
	=	Vertical layout	
	=	Side layout	

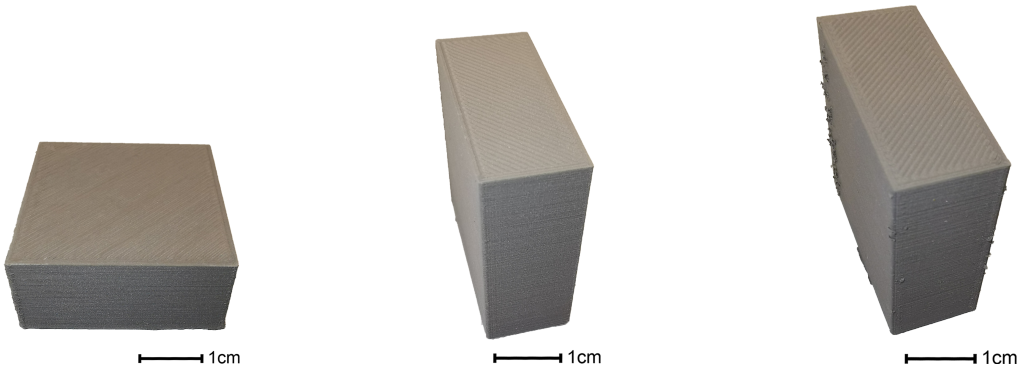

(a) Flat layout **(b)** Side layout **(c)** Vertical layout

Figure 28: The green CT specimens.

4.2.4 Surface defects

During the printing process, several defects were observed on the surfaces of the specimens. Hence, further parameter experimentation was necessary to eliminate

the defects and achieve excellent surface quality. The figures in this section contain different types of defects presented by metal printing. Note that these specimens were disposed and not used for mechanical testing.

When printing with insufficient initial layer height, cracks occur on the first layer for the tensile and fatigue specimens. The cracks are apparent at the inner walls and propagating in the infill, as seen in Figure 29.

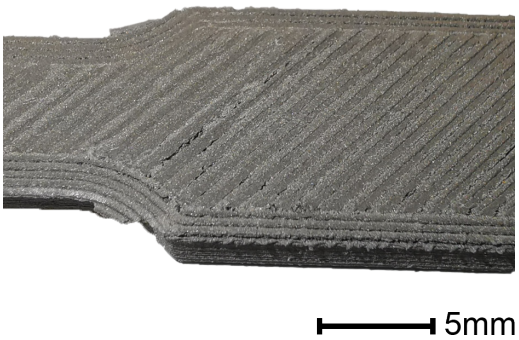

Figure 29: Cracks are observed on the first layer of the tensile specimen.

The CT specimens are especially prone to localized surface deformation. The deformation is shown by irregular wall structures where the material is deposited in a non-linear pattern. This results in inconsistencies which can alter the geometry of the specimen, as seen in Figure 30.

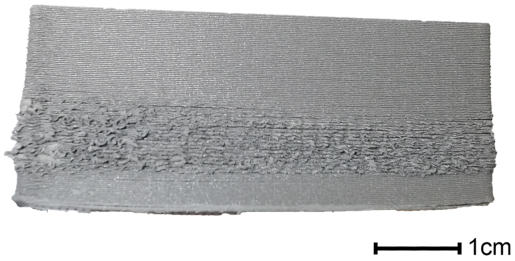

Figure 30: Deformations are observed on the walls of the flat CT specimen.

Gaps between the strands on the top layer of a specimen are an occasional occurrence and most visible on tensile specimens. In Figure 31, the gaps are visible as dark voids between strands in the gauge area. These gaps are also observed inside the specimens during printing.

Figure 31: Gaps between strands are observed on the top layer of the tensile specimen.

Poor adhesion between layers (delamination) is specifically a problem for CT specimens. Instead of merging, forming one consistent bulk material, the layers are separated and warping. From Figure 32, the poor layer adhesion is especially noticeable on the corners of the CT specimens and less visible when approaching the center of the walls.

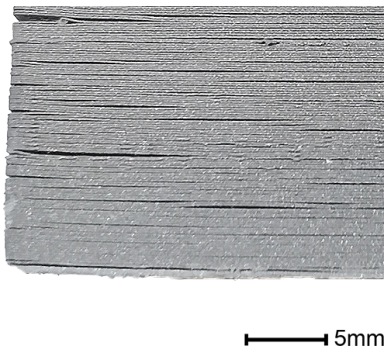

Figure 32: Delamination is observed for the CT specimens.

On some specimens, small deposits of excess material are observed on the outer walls. As seen in Figure 33, this occurs at the same spot for each layer, most notably for the vertical CT specimens. The defect is less prevalent on tensile and fatigue specimens.

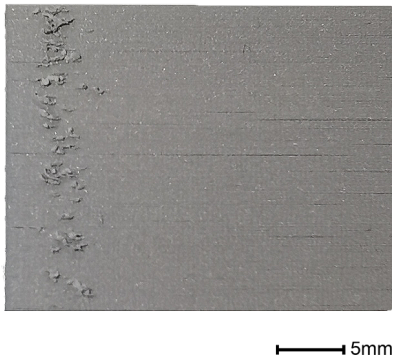

Figure 33: Some excess material is observed on the walls of the vertical CT specimen.

High roughness and uneven surfaces are especially prevalent on CT specimens, as shown in Figure 34. That is especially noticeable when increasing the layer height.

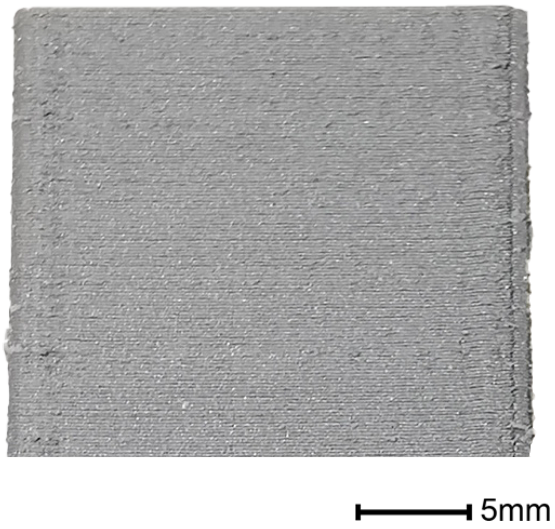

Figure 34: Some roughness is observed on the walls of the side CT specimen.

From Figure 35, the first layer of the tensile specimen is observed to be uneven. This is noticeable for all specimens, but more prevalent for the tensile and fatigue specimens.

Figure 35: Some uneven first layers are observed for the tensile specimen.

Figure 36 shows the bottom surface of a flat CT specimen. The center of the first layer exposes the infill, which otherwise should be covered by a bottom layer. This is especially prevalent for the flat CT specimens due to the larger surface area to the bed.

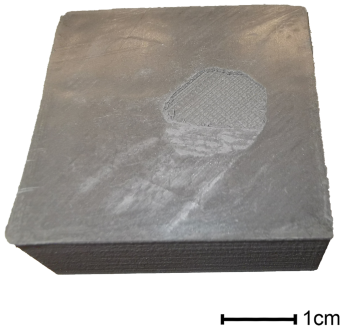

Figure 36: Tearing is observed on the first layer of the flat CT specimen which exposes the infill.

Warping is a frequent occurrence for all specimens when not using optimal parameters. As seen in Figure 37, the corners of the specimen lift from the build plate during printing.

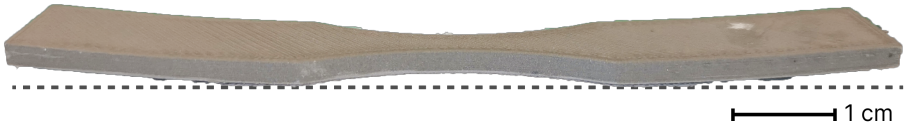

Figure 37: Warping is observed as the corners of the specimen lift from the horizontal surface, represented by the dashed line.

4.3 Debinding and sintering

4.3.1 Tensile specimens

The green parts undergo debinding and sintering, and as a result, shrinkage (Figure 38). Hence, the dimensions of the specimens decrease post-sintering. Table 17 addresses the average dimensions of the tensile specimens pre and post-sintering, as well as the shrinkage percentages from the densification during sintering.

Table 17: The average dimensions of the tensile specimen before and after sintering.

Dimensions of the tensile specimen			
Dimension	**Pre-sintering [mm]**	**Post-sintering [mm]**	**Shrinkage [mm]**
W	7.35	6.03	-1.32
T	3.57	2.80	-0.77
L	118.84	98.73	-20.11

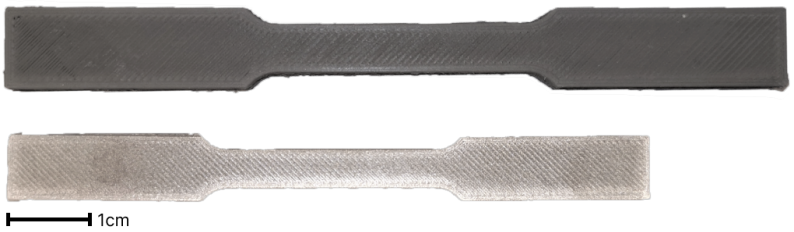

Figure 38: The green part on top and the sintered specimen on the bottom.

4.3.2 Fatigue specimens

Table 18 shows the average dimensions of the fatigue specimens pre and post-sintering, in addition to the shrinkage percentages due to the densification during sintering. The shrinkage of the specimen is shown in Figure 39.

Table 18: The average dimensions of the fatigue specimen before and after sintering.

Dimensions of the fatigue specimen			
Dimension	**Pre-sintering [mm]**	**Post-sintering [mm]**	**Shrinkage [mm]**
W	5.07	4.12	-0.95
T	2.42	1.92	-0.50
L	91.67	75.78	-15.89

Figure 39: The green part on top and the sintered specimen on the bottom.

4.3.3 CT specimens

Table 19 shows the average dimensions of the CT specimens pre and post-sintering, in addition to the shrinkage percentages due to the densification during sintering. The shrinkage of the specimens is shown in Figure 40.

Table 19: The average dimensions of the CT specimen before and after sintering.

Dimensions of the CT specimens			
Dimension	**Pre-sintering [mm]**	**Post-sintering [mm]**	**Shrinkage [mm]**
H	35.77	28.89	-6.88
T	15.50	12.14	-3.36
L	37.13	29.96	-7.17
H	36.98	28.58	-8.40
T	15.71	12.66	-3.05
L	36.16	29.56	-6.57
H	35.55	29.14	-6.41
T	15.77	12.69	-3.08
L	37.57	29.35	-8.22
	=	Flat layout	
	=	Vertical layout	
	=	Side layout	

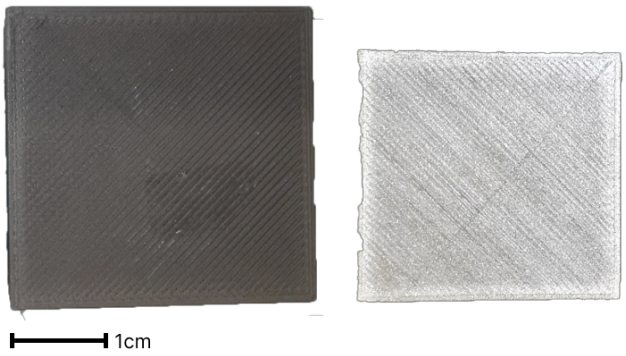

Figure 40: The flat green specimen to the left and the flat sintered specimen to the right.

4.3.4 Shrinkage

The relation between the average post- and average pre-sintered dimensions is calculated to obtain the shrinkage percentages. The shrinkage percentages for each specimen are shown in Figure 41 and 42. The specimen types are split into two figures with their respective dimensions. The error bars in the figures are set using the statistical approach to calculate the standard deviation.

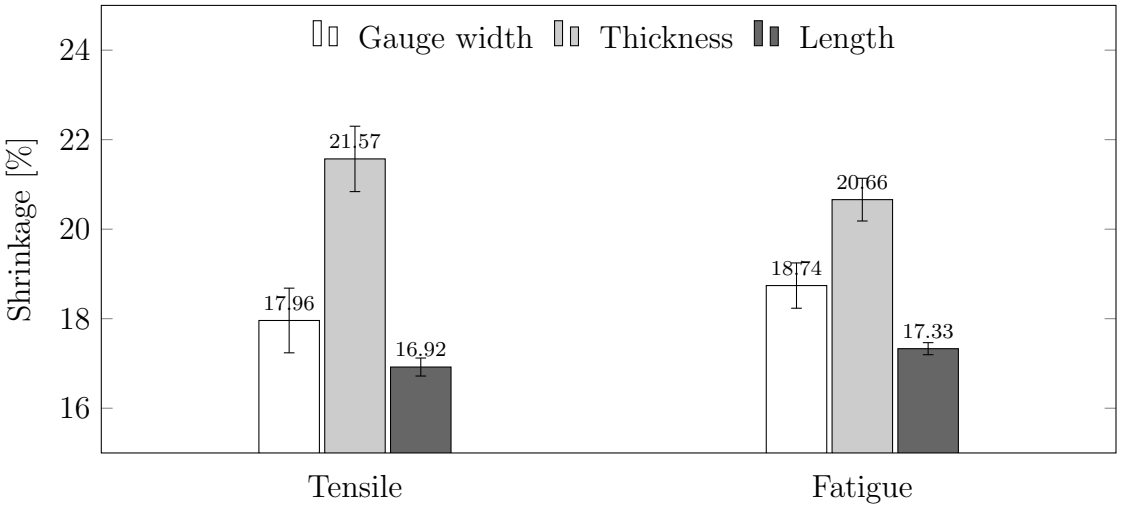

Figure 41: The average dimension shrinkage of the tensile and fatigue specimens represented by a bar plot. The addressed dimensions are the gauge width, W, thickness, T, and length, L.

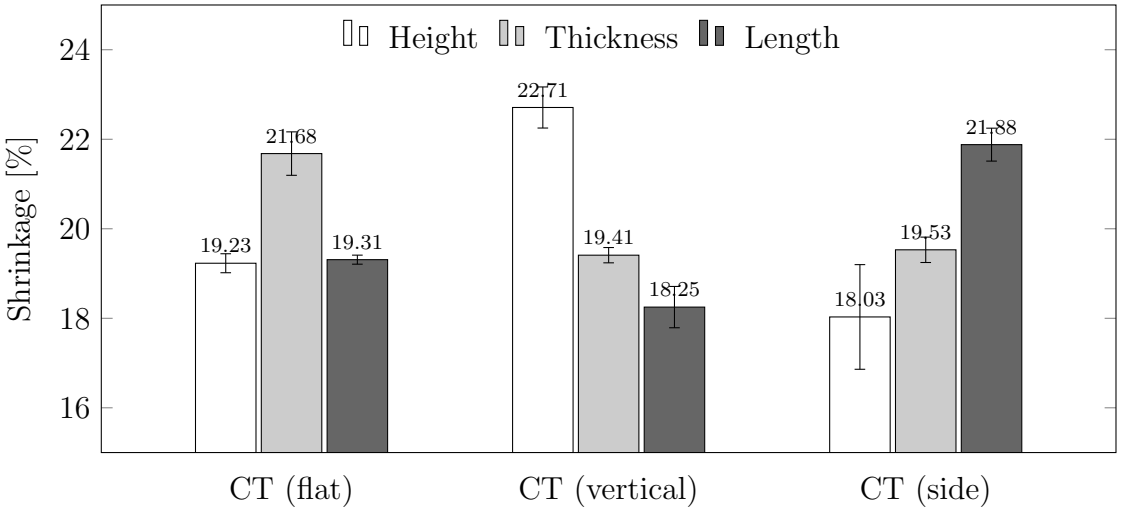

Figure 42: The average dimension shrinkage of the CT specimens represented by a bar plot. The addressed dimensions are the height, H, thickness, T, and length, L.

4.3.5 Mass loss

During debinding, the polymer binder is extracted from the green parts, resulting in a mass loss. The average mass of the specimens before and after post-processing treatment is shown in Table 20, and Figure 43 shows the average mass loss of each specimen type.

Table 20: The average mass of the specimen types before and after sintering.

Mass comparison of specimens			
Specimen	**Pre-sintering** [g]	**Post-sintering** [g]	**Δmass** [g]
Tensile	20.22	17.49	-2.73
Fatigue	10.48	9.33	-1.15
CT (flat)	92.51	81.66	-10.85
CT (vertical)	93.32	81.78	-11.54
CT (side)	93.77	82.09	-11.68

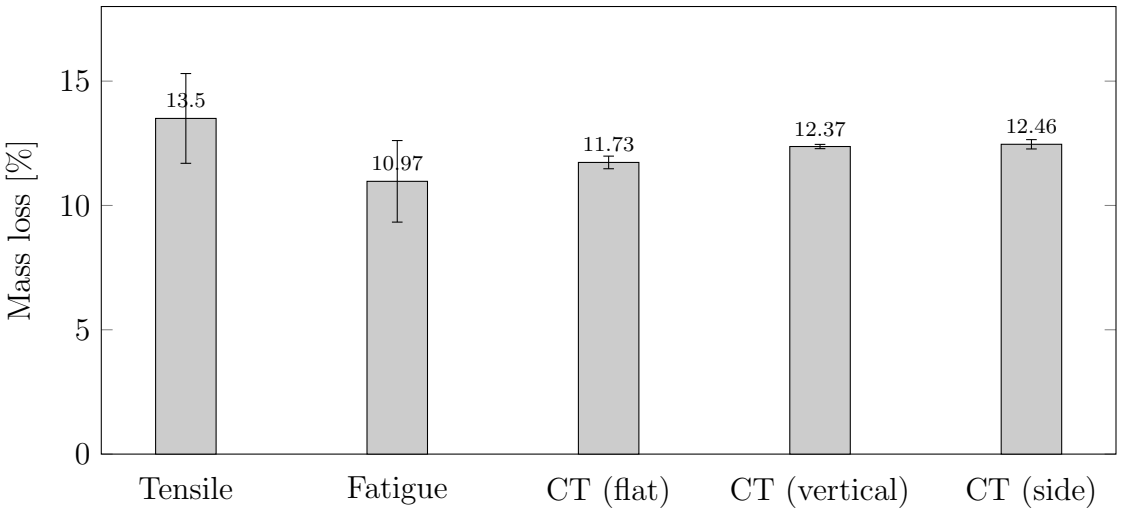

Figure 43: The average mass loss of each specimen type due to debinding and sintering.

4.4 Mechanical testing of sintered specimens

4.4.1 Fatigue testing

The sintered fatigue specimens are put under uniaxial fatigue loading. The stress amplitude, σ_a, and the number of cycles to failure, N_f, are tabulated and plotted for each specimen in order to make the S-N diagram (Table 21 and Figure 44). The maximum number of cycles set during testing is 2,000,000, and when a specimen exceeds the maximum value, the test is stopped. The stress amplitude at which the specimen exceeds 2,000,000 cycles is called the fatigue limit. An arrow is added to the point, signifying that the fatigue life may be longer than represented. The specimens fracturing at σ_a=300MPa, σ_a=200MPa, and the two run-out specimens,

σ_a=100MPa, and 80MPa are excluded when calculating the trendline. They are excluded due to 300MPa and 200MPa fracturing in LCF ($< 10^4$ cycles), and the run-outs exceeding the maximum limit at 2,000,000 cycles. That is due to the Basquin equation (Equation 4.1) not being applicable in those regions. Using the equation, and the formula of the trendline (Equation 4.2), the fatigue properties of the specimen are acquired (Table 22). In addition, confidence intervals are added to the HCF data ($\geq 10^4$ cycles) to estimate the uncertainties. 95% confidence implies that 95% of estimated data are below the line, and 5% of all estimated data below the 5% confidence line.

$$\sigma_a = \sigma'_f(2N_f)^b \tag{4.1}$$

$$\sigma_a = 476.12(2N_f)^{-0.114} \tag{4.2}$$

Table 21: The experimental data from the fatigue testing. The mean stress, σ_m, is calculated using the set stress amplitude, σ_a, and the stress ratio, $R = 0.1$. The number of cycles to failure, N_f, is obtained as the specimen fractures.

Experimental fatigue data		
$\sigma_\mathbf{a}$ **[MPa]**	$\sigma_\mathbf{m}$ **[MPa]**	$\mathbf{N_f}$ **[cycles]**
300	366.67	523
200	244.44	1,987
150	183.33	40,556
150	183.33	87,690
130	158.89	30,594
130	158.89	69,594
120	146.67	241,278
100	122.22	421,044
100	122.22	≥2,000,000
80	97.78	≥2,000,000

Table 22: The Basquin constants of the specimens acquired by the experimental fatigue data.

Fatigue properties			
Property	**Symbol**	**Value**	**Unit**
Fatigue strength coefficient	σ'_f	482	MPa
Fatigue strength exponent	b	-0.115	-

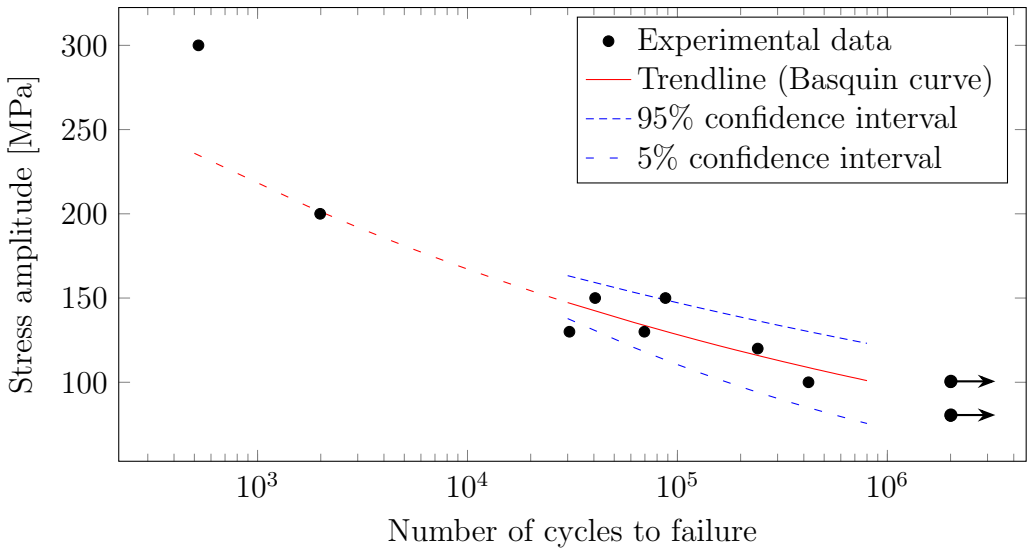

Figure 44: The number of cycles to failure at a given stress amplitude is given by a scatter plot where each point represents one fatigue specimen. The solid red trendline is calculated for the HCF data with an upper and lower confidence interval. The dashed red line in LCF is an extension of the trendline.

4.4.2 Fractography with low stress specimen

All figures in this section are SEM images of the fracture surface of the fatigue specimen with the longest fatigue life (excluding run-outs). The specimen with the longest fatigue life is at σ_a=100MPa with 421,044 cycles to failure. This specimen is chosen since it has the most visible fatigue characteristics. The fracture surfaces of the other specimens are shown Section 4.4.3 and Appendix A.

Figure 45 shows the total area of the fracture surface and the locations of Figure 47, 48, and 49, in addition to the printing direction. These locations are chosen to show a crack initiation, propagation, and fracture site. Multiple internal voids are observed between strands/layers. Also, Figure 46 shows the same fracture surface,

but the crack propagation sites and pores are outlined in red and blue, respectively.

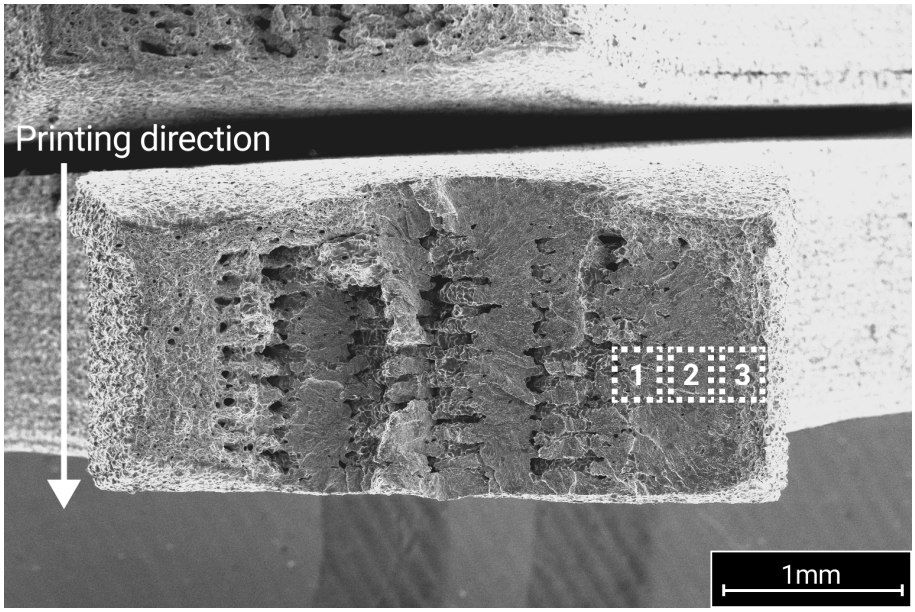

Figure 45: The overview of the fracture surface - 40x magnification. 35.3mm working distance. 20kV voltage.

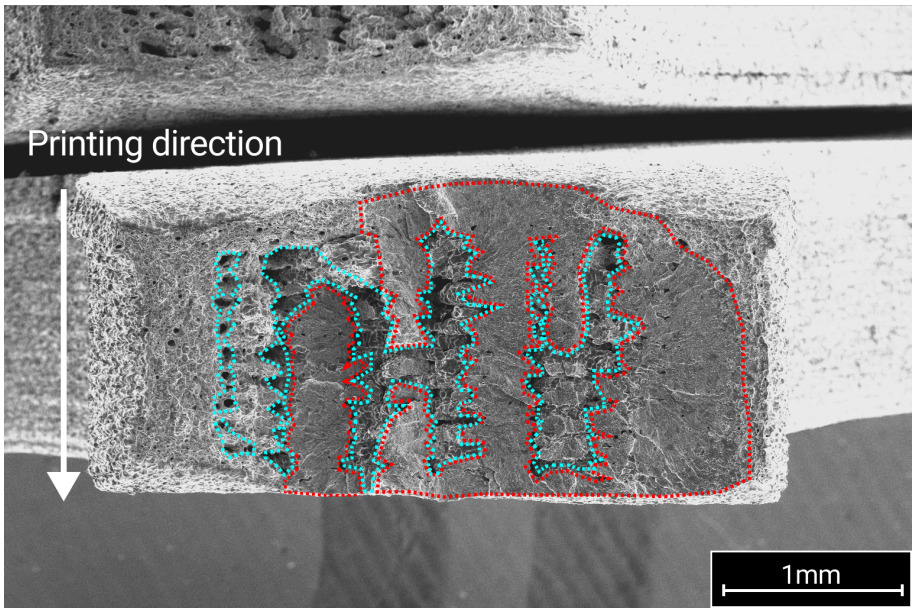

Figure 46: The crack propagation sites outlined with red, and macropores outlined with blue - 40x magnification. 35.3mm working distance. 20kV voltage.

Figure 47 shows area 1 from Figure 45. It shows the crack initiation site from an internal macropore (highlighted in red) and the corresponding crack propagation directions (marked with red arrows). It is observed that the cracks originate from the macropore and propagate outwards in the material. The pore structure is easily distinguished from the rest of the microstructure due to its smooth appearance.

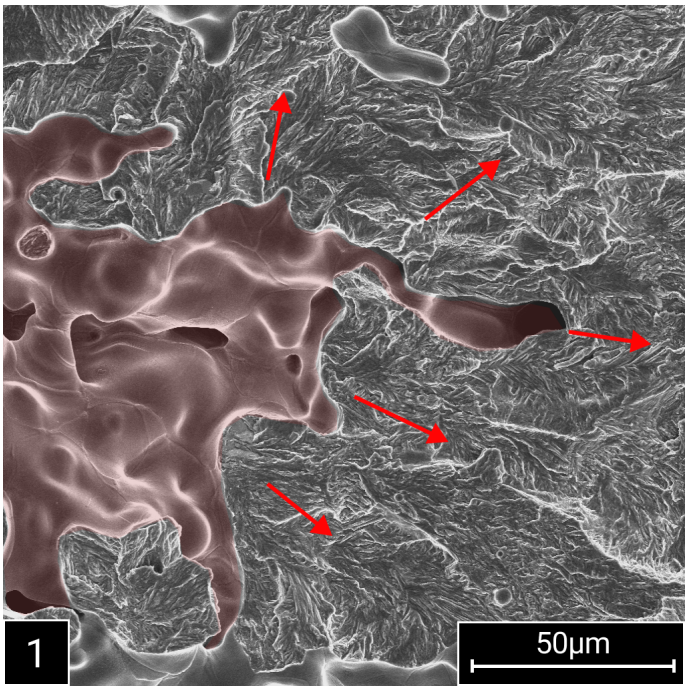

Figure 47: The crack initiation site - 500x magnification. 35.2mm working distance. 20kV voltage.

Figure 48 shows area 2 from Figure 45, where stable crack growth occurs. Multiple micropores are observed on the crack surface. These are separated from the macropores in Figure 47 due to their circular appearance and smaller diameter.

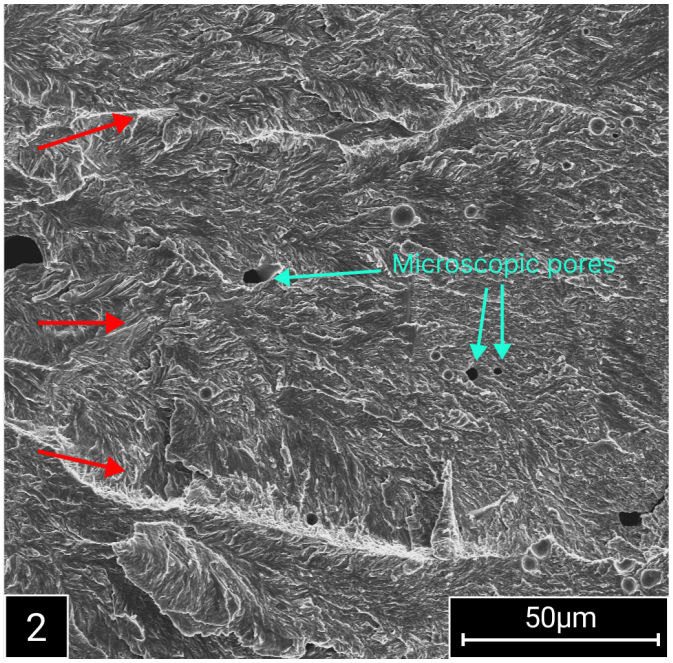

Figure 48: The stable crack propagation site - 500x magnification. 35.2mm working distance. 20kV voltage.

Figure 49 shows area 3 from Figure 45, which is the fracture site. The area marked with red shows the transition zone, where the crack propagation becomes unstable. It also displays the transition from crack propagation to final fracture. The green zone shows the final fracture surface of the specimen. Ductile dimples are observed covering the entirety of the final fracture surface.

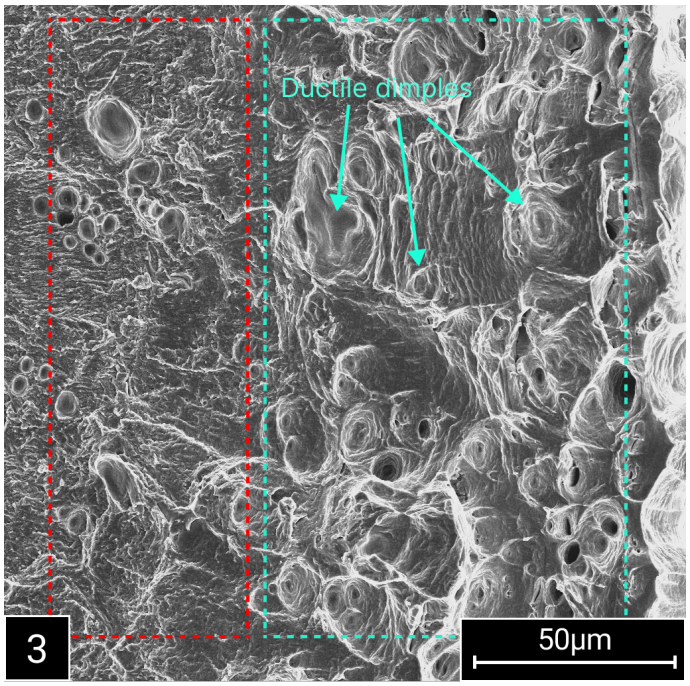

Figure 49: The final fracture site - 500x magnification. 35.2mm working distance. 20kV voltage.

Figure 50a shows individual grains in the microstructure. It shows the smooth surface of a macropore where the grains are easily distinguished. The grain boundaries are visible as thin lines on the pore surface. The diameter of an arbitrary grain is measured to get an idea of the average grain size within the material.

Figure 50b shows a micropore in the material. The pores are visible as circular voids in the material. The diameter of a micropore is measured to get an idea of the average micropore size in the material.

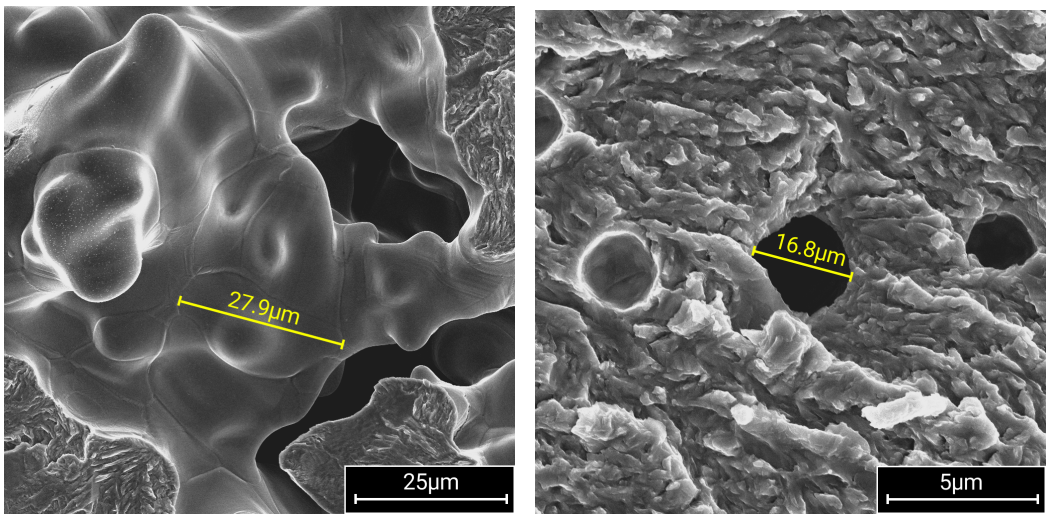

(a) Grain diameter **(b)** Micropore diameter

Figure 50: Visible grains are observed on the macropore surface (left), and a micropore (right) is showcased - 1000x/5000x magnification. 35.2mm/35.2mm working distance. 20kV voltage.

4.4.3 Fractography with higher stress specimens

Figure 51 shows the fracture surface of the fatigue specimen with medium stress amplitude, $\sigma_a = 200$MPa and $N_f = 1,987$ cycles to failure. Also, Figure 52 shows the fracture surface of the fatigue specimen with the shortest fatigue life, which is the specimen at $\sigma_a = 300$MPa with just N_f=523 cycles to failure. These specimens are chosen to compare the fracture surfaces at higher stress amplitudes with the fracture surface of the specimen at low amplitude (Section 4.4.2). In Figure 51, the magnified image is magnified to 500x to show the small propagation sites. In addition, red arrows are added to display the crack propagation directions. However, no crack propagation sites are observed in Figure 52, and the fracture surface is covered in ductile dimples and pores.

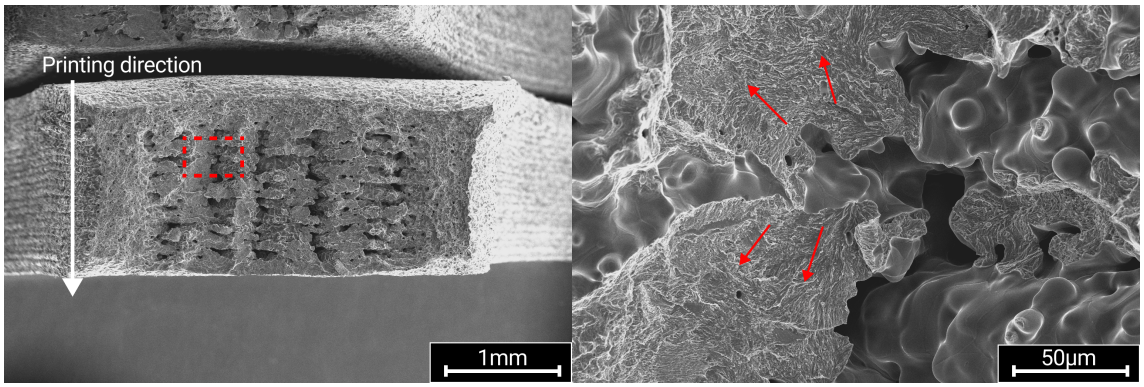

Figure 51: σ_a=200MPa, N_f=1,987 cycles to failure - 40x / 500x magnification. 14.4mm / 14.4mm working distance. 20kV voltage

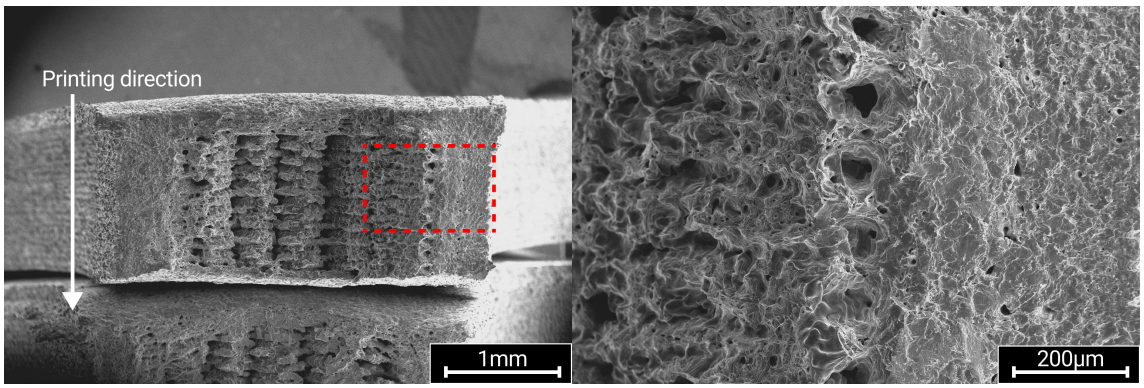

Figure 52: σ_a=300MPa, N_f=523 cycles to failure - 40x / 200x magnification. 12.4mm / 11.4mm working distance. 20kV voltage.

4.4.4 Tensile testing

The sintered tensile specimens are put under uniaxial tensile loading. Multiple mechanical properties are obtained by tensile testing, which is represented in Table 23. The elastic modulus, E, is calculated by dividing the maximum stress by the maximum strain in the linear elastic region. The 0.2% offset yield strength, $\sigma_{y,0.2\%}$, is set to the stress value at 0.2% elongation, and is a valid estimate for the yield strength of the material. The ultimate tensile strength, σ_{UTS}, is the maximum stress level of the specimen before necking. Finally, the total elongation at fracture, ε_{tot}, includes both the total elastic and total plastic strain to failure. Figure 53 shows the stress-strain behavior of the tensile specimens. In addition, Figure 54 shows the deformation of the specimens during tensile loading, including the lateral strain distribution.

Table 23: The average tensile properties of three tensile specimens. The values are obtained from Figure 53.

Tensile properties				
Property	**Symbol**	**Value**	$\sigma_{\mathbf{std}}$	**Unit**
Elastic modulus	E	120	±17	GPa
0.2% offset yield strength	$\sigma_{y,0.2\%}$	142	±10	MPa
Ultimate tensile strength	σ_{UTS}	432	±17	MPa
Total elongation at fracture	ε_{tot}	0.52	±0.07	-

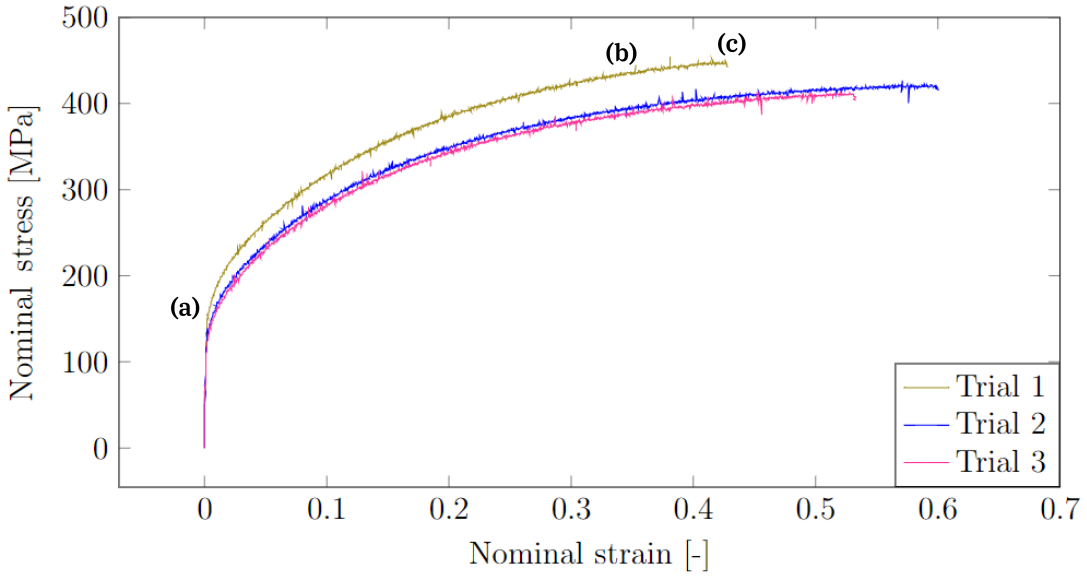

Figure 53: The nominal stress versus nominal strain is shown for three trials of tensile testing. All specimens show linear elastic behavior initially, and the end-points of the graphs show the fracture points of the specimens.

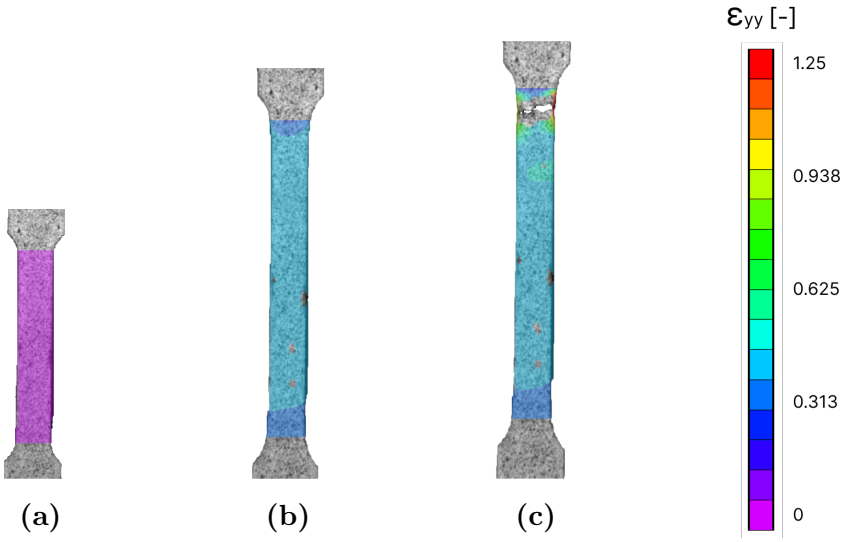

Figure 54: The specimens at three stress/strain levels of Trial 1, shown in Figure 53. **(a)** shows the specimen at the end of the linear elastic region before yielding. **(b)** is the specimen when approaching UTS, and **(c)** shows the fracture of the specimen. The colors on the specimens represent the distribution of axial strain, ε_{yy}, on the specimen surface at the given stress magnitude.

5 Discussion

5.1 The printing process

The printing parameters found in Table 12 and 13 are specifically selected to optimize the surface and internal quality of the specimens. That implies that outer defects such as roughness, cracks, deformation, delamination, swelling, warping, and gaps between strands should be minimized to obtain optimal mechanical performance. The internal defects, pores, inconsistencies, impurities, and poor structure have a huge influence on the mechanical properties and thus should be eliminated. The optimal process parameters are acquired using the optimal parameters from the specialization project as a basis and implementing more changes as the specimen geometries advance. In the project, hollow specimens and small solid specimens were printed to analyze which parameters influenced the quality. It was proven for the small specimens that the number of defects was greatly reduced by increasing the nozzle temperature and decreasing the layer height and infill printing speed. However, the tensile, fatigue, and CT specimens require more alterations for improved quality.

5.1.1 Elimination of defects

When transitioning to more advanced geometries, such as the tensile and fatigue specimens, the specialization project's parameters are not sufficient to optimize the quality. Due to their oblong shapes and low contact area, warping is especially prevalent (Figure 37). Small specimens adhere better to the build plate than their larger counterparts. This is because material shrinks during cooling, and smaller specimens have a smaller contact area where shrinkage occurs. There is an approximately 195°C temperature difference (190°C for the CT specimens) between the nozzle and the bed. That means that the bed temperature is not high enough to keep the material in a semi-liquid state, and the material is solidified. During solidification, the bottom layers contract as the material shrinks, which is frequently observed on corners, and the bottom part of the specimen begins to lift from the bed. The lifting results in uneven geometry and bending of the specimens, which significantly decreases the mechanical performance. The specimens are printed with a brim to increase the contact area to prevent warping. Although the brim is an essential tool, additional measures are paramount. Thus, a printing glue is applied to increase adhesion further. Warping is practically negligible for the tensile and fatigue specimens when using a brim with decent width and printing glue. The bed

temperature and brim width are increased for the CT specimens since the previously mentioned solutions were insufficient to eliminate warping. Increasing the bed temperature increases the flowability of the first layer and decreases the temperature difference between the nozzle and the bed. Thus, eliminating warping of the CT specimens.

When removing the specimens from the build plate after being submerged in water to dissolve the glue, tearing is an issue. Tearing occurs when the specimens are removed prematurely before the glue is dissolved. As a result, chunks of the material are deposited on the build plate after removal, and the inner structure of the specimen is exposed (Figure 36). The tearing makes the specimen unsuitable for further testing, since the defect will act as a huge crack initiation site, and significantly decrease the mechanical properties. The specimens are left for several hours, preferably overnight, in warm water to dissolve the glue and prevent tearing. Heated water accelerates the dissolving of the glue, and it is swapped out frequently to decrease the glue concentration in the water. Then, the specimens should loosen themselves from the build plate. If the specimens still adhere to the plate, the glue is not dissolved, and no physical removal should be performed. Subjecting the specimens in water is possible since the material is non-hygroscopic. That means that the material does not absorb water or humidity, and the steel particles are not affected [36].

Gaps between strands are observed in the early printing of tensile specimens. From Figure 31, gaps between strands are visible as dark spots where the strands are disconnected. By observation during printing, the gaps appear internally in the specimens as well as on the surface. In other words, when a specimen contains multiple surface gaps, there is a high number of defects internally. If not improved, the disconnected strands greatly weaken the ability of the material to withstand mechanical loadings. Since the strands are separated, they will easily be pulled apart and cause premature failure. By increasing the nozzle temperature to 295°C for tensile/fatigue specimens and 290°C for CT specimens, the flowability of the material is increased, and the strands are fused. The temperature increase and lower printing speeds, 30mm/s for all specimens, are the main factors influencing the strand adhesion in the specimens. It could be speculated that increasing the printing speed increases the merging of strands since the strands still remain in a semi-liquid state as the next strand is deposited. However, increasing the speed resulted in internal inaccuracies, which increased the porosity. Also, the cooling fan percentage is decreased from the default 100% to 50% to keep the material in a semi-liquid state for a longer time and to encourage strand fusion. For the initial layer, the cooling

fan percentage is set to 0% to secure a proper foundation by further encouraging fusion. Increasing the flow rate to a maximum of 115% does not greatly influence the specimen quality. Contrary, it may result in overextrusion and surface deformations (Figure 30). The deformations are caused by extruding too much material over a dedicated area. The overextrusion causes many irregularities in the layers, especially on the outer walls, and gives the specimen an inconsistent outer appearance. Thus, the flow rate multiplier is kept at default 100%. It is observed in multiple articles about FDM that increasing the flow rate multiplier is a solution to eliminate gaps and internal pores of specimens. However, it is not a valid solution for the specimens in the thesis, and may be due to the composite filament behaving differently to other filaments. In future work, small modifications to the multiplier should be performed to observe gap elimination without causing overextrusion. On some occasions, gaps are observed between the inner wall and the infill. This is solved by increasing the infill overlap percentage from 0% to 10%. Finally, the skin overlap percentage is set to 30% since the top, and bottom surfaces require some additional overlap to ensure true filling.

In some instances, cracks develop on some sides of the specimens (Figure 29). That is a rare occurrence and is differentiated from gaps between strands. While gaps are located between the strands with equal length and distance from another, cracks may intersect the strands and do not have the same repeated pattern. Usually, this is a result of too low layer height. When the layer height is below a certain threshold, <0.1mm in this situation, some of the material struggles to adhere to the previous layer/build plate and bounces back to the outer nozzle surface. This results in the rupture of strands, which causes cracks in layers. By increasing the infill layer height to 0.1mm or higher, all material adheres to the previously deposited layer due to the increased weight and surface area of the strands. However, this is still a problem for the initial layer. Even with glue, the initial layer height is increased to 0.2mm (0.15mm for the CT specimens) to ensure proper adhesion. Hence, increasing the initial layer height is important to obtain a good and uniform foundation for the rest of the specimen.

While an increased layer height is beneficial in eliminating certain defects, it also introduces increased surface roughness and 'stair effect' on the sides (Figure 34). The roughness introduces sharp corners to the surface, which may act as crack nucleation sites depending on the loading direction. Therefore, a smooth surface is necessary to minimize crack nucleation and the probability of early fracture. As the layer height increases, so does the width/height of the strands. As the strands enlarge,

the layers in the specimen are more easily observed. The specimens give a smoother appearance with lower layer height and lower roughness. Too low layer height also results in poor adhesion to previously deposited layer/build plate. The infill layer height is set to 0.1mm for all specimens, which is the optimal value to ensure proper adhesion and minimal surface roughness. Still, some roughness is observed on the green parts but is less noticeable after post-processing treatment as the specimens shrink.

The quality of the initial layer is crucial for the overall quality. That is since it acts as the foundation of the specimen. However, the build plates tend to swell after a certain number of prints. The swelling is observed as minor lumps on the bed. As a result, when specimens are printed, the lumps from the plate are transferred to the specimens, as shown in Figure 35. These irregularities propagate into the material and harm the internal structure. This is caused by the material's high temperature (290-295°C), which significantly degrades the build plate. Several solutions are introduced to solve this problem. First, the build plates are swapped regularly to avoid heat build-up on the plate surface. Another solution is to move the printing of the specimen to another area of the plate. Finally, sturdier build plates dedicated to printing metal specimens may be utilized. While printing the tensile, fatigue, and CT specimens in the thesis, swapping of plates and moving of the specimens are performed.

Table 13 shows that alterations are made to the printing configuration of the CT specimens. Compared to the tensile and fatigue configuration, the nozzle temperature decreases from 295°C to 290°C, and the bed temperature increases from 100°C to 110°C. The initial layer height is decreased from 0.2mm to 0.15mm. Due to technical issues with the original printer after printing the tensile and fatigue specimens, another Prusa i3 MK3 is utilized when printing the CT specimens. For this printer, the nozzle temperature is more unstable with higher fluctuations from the set value, which means that printing at 295°C resulted in temperature errors due to exceeding the maximum limit of 300°C. When the limit is reached, the print stops and must be restarted. Due to limited time, it was decided to continue with decreased nozzle temperature (290°C) to reduce the risk of causing an error. Also, the brim width and bed temperature are increased to reduce the CT specimens' warping. Increasing the brim width increases the bed's surface area, and the bed temperature is elevated to ensure the flowability of the material and improve the fusion of strands. In addition to warping, some delamination is observed on the CT specimens using the printing configuration for the tensile and fatigue specimens (Figure 32). This is especially

prevalent between the initial layer and the bulk of the material. Thus, the issue is solved by decreasing the initial layer height from 0.2mm to 0.15mm to equalize the height difference between the first and second layers. By adjusting the layer height, the CT specimens are more homogeneous in structure, and delamination is eliminated. However, 0.2mm initial layer height is still required for the oblong tensile and fatigue specimens to reduce rupture of strands and to improve the initial layer quality.

5.2 Post-processing treatment

5.2.1 Mass loss due to debinding

During debinding, the specimens undergo substantial mass loss as the polymer binder exits the material. Theoretically, all the polymer should leave the material, resulting in pure steel specimens. That implies that the total weight of the specimens after debinding is the weight of the steel powder in the green parts. From Table 20 and Figure 43, it is observed that the CT specimens (flat: -10.85g, vertical: -11.54g, side: -11.68g), undergo a higher average mass loss than the tensile (-2.73g) and fatigue specimens (-1.15g). That is obvious since the CT specimens have a larger initial mass, and because the original filament is $>$ 80wt% steel particles and $<$ 20wt% polymer, more polymer is evaporated. However, percentage-wise, there is little deviation in mass loss across the CT specimen types from Figure 43. That proves that the mass loss percentage is independent of the printing orientation for the CT specimens. Still, the error margins for the tensile and fatigue specimens are distinctive due to the number of specimens used to calculate the percentages. The weights of five and 12 specimens calculate the average mass loss percentage for the tensile and fatigue specimens, respectively. However, only three, two, and three specimens are used to calculate the flat, vertical, and side CT specimens. Therefore, the error margins for the CT specimens are not accurate representations of the total picture. Thus, to obtain accurate and precise data with appropriate margins, more specimens should be used for calculations.

5.2.2 Shrinkage due to sintering

The specimens undergo significant shrinkage during sintering. According to Ultrafuse [35], the material shrinks 19% in the x and y-direction and 21% in the z-direction. The specimens in the thesis are designed with this shrinkage in mind. Thus they are printed 19%/21% larger than the desired dimensions. After receiv-

ing the sintered specimens, the percentages differ slightly from the base values. The gauge width and the length of the tensile specimens, which are the dimensions in the x/y-plane, shrink 17.96% and 16.92%, respectively (Figure 41). That is a difference of -1.04% and -2.08% from the theoretical values. The thickness in the z-direction is slightly larger than the base value with an additional +0.57%. Likewise, the fatigue specimens' gauge width and length experience less shrinkage than the base value (-0.26% and -1.67%, respectively), and the thickness is +0.34% larger. In conclusion, the tensile and fatigue specimens' shrinkage deviation is small but not negligible.

The CT specimens are divided into three parts depending on the build orientation: flat, vertical, and side. From Figure 42, it is noticeable that the shrinkage varies between the specimen types. In terms of thickness (z-direction), there is a 1.03% difference between the most significant and smallest shrinkage. On the x/y-plane, the dimensions are moderately close to the theoretical values, with the highest deviation at -0.97% from the theoretical shrinkage value. Shrinkage differences are expected when discussing the tensile and fatigue specimens due to different geometries. However, it may be discussed that the differences between the CT specimens originate from the build orientation. Also, variations in the sintering process may be another factor. During printing, it was made clear that the CT specimen types possess different internal and surface qualities. Therefore, one type may have a higher density than another, which may affect the shrinkage. Due to limited time and technical issues, precise density measurements are not performed for the specimens to validate the assumption. Also, it is observed that the shrinkage of the CT specimens follows the theoretical values better than the tensile/fatigue specimens. Hence, one can assume that the values given by the supplier are most suited for thicker specimens.

5.3 Mechanical testing and analysis

5.3.1 Fatigue properties as a result of microstructure

The fatigue data of 10 tested fatigue specimens (Figure 44) show an increase in cycles to failure as the stress amplitude decreases. The is elongation/compression of the specimens decreases with decreasing stress amplitude. That implies that the specimens tolerate more cycles to failure compared to higher amplitudes. In addition, when crack initiation occurs, the crack propagation is drastically reduced. This proves that the data correspond to theory based on the Basquin equation (Equation 4.1), where decreasing σ_a increases N_f. Based on the experimental data, a trendline

is constructed using regression analysis. Four points are not taken into consideration when constructing the trendline. These are the run-out points, σ_a = 100MPa and 80MPa, and the LCF data, σ_a = 300MPa and 200MPa. That is due to the Basquin equation not being applicable for LCF or points exceeding the maximum limit of 2,000,000 cycles. Hence, the Basquin equation is applied in HCF from σ_a = 150MPa to σ_a = 100MPa (referring to the specimen at σ_a = 100MPa and N_f=421,044 cycles where fracture occurs). Moreover, the Basquin constants, σ'_f and b, are extracted from the trendline equation and represent the fatigue properties of the additively manufactured AISI 316L specimens with FDMS. The fatigue strength coefficient, σ'_f, is 482MPa, and the fatigue strength exponent, b, is -0.115. For conventional forged austenitic AISI 316L, the values are σ'_f=586MPa and b=-0.142 [46], where σ'_f is higher and b is smaller than the values obtained of the printed material. σ'_f is often approximated to be equal to the true fracture stress, σ_f, where increased σ_f equals a higher tolerance to fatigue loading. Also, a smaller b equals a longer fatigue life [47]. Thus, the specimens printed with FDMS have slightly inferior fatigue performance than regular forged AISI 316L.

It is observed that the fatigue limit, σ_f, is between σ_a = 100MPa and σ_a = 80MPa. Since one specimen at 100MPa failed before reaching 2,000,000 cycles, it is concluded that the fatigue limit is below 100MPa. The results are similar compared to specimens printed with SLM and the same build orientation. SLM specimens with a flat build orientation have a fatigue limit of 101MPa, which is a slight increase from the FDMS specimens at 80MPa$\leq \sigma_f <$100MPa [48]. This shows that the fatigue limit obtained is reasonable compared to similar additive manufacturing techniques. However, an exact fatigue limit for FDMS could be obtained by testing more fatigue specimens to acquire more data.

It is observed that eight specimens enter HCF ($\geq 10^4$cycles). The transition from LCF to HCF occurs at a stress amplitude $\leq$150MPa, theoretically indicating a transition from surface-initiated cracks to internal cracks. This is true by observing Figure 45. From the cross-section fracture surface of Figure 45, three images are captured to display the fatigue characteristics of the material. From Figure 47, it is observed that the cracks nucleate at the edges of the macropores. Theoretically, defects in the material act as stress risers due to incoherence with the surrounding matrix. Figure 47 shows Stage 1 of the Paris' diagram (Figure 6) where the crack growth rate is unstable. From Figure 47, it is observed that the cracks propagate outwards from the macropore into the material. In Figure 48, the crack growth becomes stable and proceeds to propagate to the specimen surface. That marks

a transition from Stage 1 to Stage 2, following the Paris' diagram and the Paris' equation (Figure 6 and Equation 2.2). During the fatigue testing of the specimen, Stage 2 covers the majority of the crack propagation. During the transition from Stage 2 to Stage 3 of the Paris' diagram, the cracks enter the transition zone where the crack propagation becomes unstable (Figure 49). From the Paris diagram, that implies a rapid increase in crack growth rate from the stable propagation. This zone transitions into the final fracture zone, where the specimen ruptures. The final fracture zone is observed where the cracks become less noticeable and ductile dimples appear. The creation of ductile dimples is a consequence of the material being ductile during loading. As the material elongates, shelled voids enlarge and merge when coming in contact with another. That creates a rough surface with distinct asperities. Moreover, if the material is brittle, the final fracture surface will have a drastically different morphology. Instead of dimples, sharp cleavage structures cover the final fracture surface. However, no cleavage structures are observed on the fracture surface, indicating that the material is ductile.

When observing the fracture surface of a specimen at higher stress amplitude, crack propagation is less present. At σ_a = 200MPa and N_f=1,987 cycles to failure in Figure 51, the crack propagation sites are drastically smaller than in Figure 48. The number of cracks is greatly reduced, and fewer flat surfaces cover the fracture surface. The distance from propagation to the transition site is also reduced as the final fracture occurs earlier than in Figure 49. That shows that as the number of cycles to failure decreases with increasing stress amplitude, the specimens exhibit less fatigue behavior. This is prevalent in Figure 52 with σ_a = 300MPa and N_f=523 cycles to failure. As the stress amplitude increases from 200MPa to 300MPa, the number of cycles is reduced from 1,987 to 523. In addition, no crack propagation sites are visible, and the entire fracture surface is covered in ductile dimples. The surface roughness is also increased, with no flat surfaces observed. That proves that as the specimens fail in LCF, the specimen exhibit less fatigue behavior, which contributes to the fact that the Basquin equation is not applicable.

The observation that the material is ductile is further strengthened by the average grain size, seen in Figure 50a. The figure shows the surface of a macropore, where the grains are easily distinguished. The grains are observed to have grain size values of approximately the same order of magnitude, which implies that there is little deviation in grain diameter. One of the grains is observed to have a diameter of 27.9µm. That implies that the material primarily consists of large grains, which validates that the material is ductile. Hence, the poor fatigue properties are a consequence

of the microstructure and the grain sizes. With larger grains, the cracks have a larger area to propagate before hitting a grain boundary. If the material predominantly consists of small grains, the grain boundary density increases, decreasing the crack growth rate. The grain size is a direct result of the post-processing treatment, which encourages grain growth during sintering. However, the details of the post-processing treatment are beyond the scope of this thesis, but it remains a possible cause of the poor fatigue properties.

In addition, Figure 48 and 50b shows that multiple micropores are present in the material. The micropores are separated from the macropores (Figure 47) primarily for their smaller and spherical geometry. Additionally, the macropores primarily exist between strands and layers, while the micropores exist within the material. One micropore is measured at 16.8µm, which is considered to be a large micropore. Normally, these pores can be detrimental to the material's mechanical properties since they act as stress risers. However, due to the presence of larger macropores between strands and layers, the damage caused by the micropores may be less compared to the macropores.

5.3.2 Tensile properties as a result of microstructure

The statement that the specimens are ductile was also observed when performing the tensile testing. When setting the grip pressure to the default 60bar, the gripping caused deep indentations on the tensile specimens. The indentations penetrated the outer surface, potentially harming the internal microstructure. That increased the possibility of fracture occurring in the grip area instead of the gauge, which would affect the tensile data. Thus, the grip pressure was decreased to 30bar, which was sufficient to ensure good grip without extensive damage.

To compare the tensile properties of the specimens to the theoretical values of annealed AISI 316L, Table 23 and 3 are utilized. The elastic modulus of the material produced by FDMS is found to be 120±17GPa. That is a reduction from the typical value of 193GPa for AISI 316L not produced by AM [15]. The reduction may be due to the high ductility of the material, which causes the specimen to yield at lower stress. That is shown by the offset yield strength of the material compared to the typical yield strength. The obtained value at 0.2% strain is 142±10MPa, while the typical value is 205MPa, which proves premature yielding [15]. Moreover, the ultimate tensile strength for the material at 432±17MPa is a reduction from the typical value of 515MPa [15]. The reduction shows that the material cannot withstand the

same magnitude of loading as annealed AISI 316L. In addition, it is shown in Figure 53 that the ultimate tensile strength is close to the fracture point. That, along with Figure 54, proves that the entire gauge elongates during loading and local necking is minimal. Finally, the total elongation at fracture is 0.52±0.07. The typical value is 0.4, which confirms the high ductility of the material [15].

In order to improve the mechanical properties of the material, including fatigue properties, the porosity between strands needs to be reduced to eliminate stress risers and potential crack initiation sites. By observing Figure 46, there is sufficient merging between layers. However, within the layers, porosity occurs between strands. That may result from insufficient overlap or high temperature differences between strands which may prevent strands from merging during printing. It is speculated that the porosity may be reduced by altering some printing parameters, such as the the nozzle temperature, printing speed, cooling fan percentage and potentially the flow rate multiplier. That may increase the overlap of the strands to reduce pores and improve uniformity. Also, by altering the temperature profile of the sintering process, the grain sizes may be reduced to decrease ductility and harden the material. However, these are pure speculations and should be studied for future work to obtain precise data.

6 Conclusion

The thesis discusses the possibility of using FDMS as a solution to produce specimens for high-strength applications. The thesis procedure involves obtaining optimal printing parameters to produce green parts with minimal defects, post-process treatment, and mechanical testing. Surface defects, such as cracks, deformations, gaps between strands, delamination, excess material, high roughness, irregularities, tearing, and warping, are eliminated by altering specific printing parameters. Generally, the defects are eliminated by increasing the nozzle temperature and overlap while decreasing the printing speed and cooling fan. In addition, the layer height is optimized to improve layer adhesion while also having minimal surface roughness. Also, modifying these parameters reduces the internal porosity observed during printing.

FDMS produces three types of specimens for three mechanical test procedures. These are the tensile specimens, fatigue specimens, and three orientations of CT specimens. Due to technical issues and limited time, only tensile and fatigue testing is performed. Mechanical properties such as the elastic modulus, 0.2% offset yield strength, ultimate tensile strength, total elongation at fracture, and the Basquin constants are calculated from the tensile and fatigue tests. The acquired mechanical properties and the fractography results show that the material is very ductile. That is primarily due to the microstructure's large grains, which softens the material. It also shows that large macropores between the strands are the leading cause of crack initiation. Thus, the specimens show a slight decrease in mechanical properties compared to conventional annealed AISI 316L.

It is recommended for future work to improve the internal integrity of the specimens by monitoring the sintering process and further modifying the printing parameters. However, the results show that producing high-strength specimens using FDMS with a composite filament is possible. The thesis covers the printing parameters' advantages and disadvantages, which is valuable information for future experimentation. In addition, the acquired mechanical properties may be a foundation for future improvements to establish FDMS as a reliable method for manufacturing high strength specimens.

7 Further work

Some factors should be altered to improve the mechanical properties of AISI 316L manufactured with FDMS. The porosity between strands needs to be reduced to eliminate potential crack initiation sites. That may be performed by modifying printing parameters such as the flow rate multiplier to ensure that strands overlap. In addition, the grain size should be reduced to decrease the ductility of the specimen and increase hardness. That may be performed by adjusting the temperature profile of the sintering process. With reduced grain size, both the fatigue and tensile properties may improve. Moreover, decreasing the ductility may result in increased tensile and fatigue properties, and potentially making it comparable to annealed 316L.

Additionally, the tensile tests were performed using three tensile specimens. For future work, more specimens should be tested to obtain more data. Thus, increasing the number of tests may be statistically beneficial to obtain more precise data with less deviation.

Another issue in the thesis is the missing fracture testing. That was initially planned to be performed using the machined CT specimens. However, due to technical issues, the machining of the CT specimens was not performed, which resulted in no fracture tests. In future work, the machining of the CT specimens should be conducted if possible to acquire additional mechanical data.

Also, precise density measurements should be performed on all specimens. That was supposed to be performed using a dedicated density kit, but due to shipping issues, it was not received. By obtaining precise density measurements of the specimens, more accurate calculations may be performed when discussing the shrinkage and porosity of the specimens. Also, CT scanning could be a valuable tool for future work to analyze the specimens' internal structure and pore distribution prior to post-processing treatment.

Finally, a detailed overview of the debinding and sintering process should be received from the company. That is not given automatically by the company and thus should be requested. Hence, information of temperatures and time periods may be used to explain the microstructure and its implications on the mechanical properties.

References

[1] Samad M.E. Sepasgozar et al. “Additive manufacturing applications for industry 4.0: A systematic critical review”. In: *Buildings* 10.12 (Dec. 2020), pp. 1–35. ISSN: 20755309. DOI: 10.3390/buildings10120231.

[2] A. Savini and G. G. Savini. “A short history of 3D printing, a technological revolution just started”. In: *Proceedings of the 2015 ICOHTEC/IEEE International History of High-Technologies and their Socio-Cultural Contexts Conference, HISTELCON 2015: The 4th IEEE Region 8 Conference on the History of Electrotechnologies* (Oct. 2015). DOI: 10.1109/HISTELCON.2015.7307314.

[3] Abbas Razavykia et al. “An Overview of Additive Manufacturing Technologies—A Review to Technical Synthesis in Numerical Study of Selective Laser Melting”. In: *Materials* 13 (May 2020). DOI: 10.3390/ma13173895.

[4] P. J. Arrazola et al. “Recent advances in modelling of metal machining processes”. In: *CIRP Annals* 62.2 (Jan. 2013), pp. 695–718. ISSN: 0007-8506. DOI: 10.1016/J.CIRP.2013.05.006.

[5] A. T. Sidambe et al. “Metal injection moulding of CP-Ti components for biomedical applications”. In: *Journal of Materials Processing Technology* 212.7 (July 2012), pp. 1591–1597. ISSN: 0924-0136. DOI: 10.1016/J.JMATPROTEC.2012.03.001.

[6] K. Satish Prakash, T. Nancharaih, and V. V.Subba Rao. “Additive Manufacturing Techniques in Manufacturing -An Overview”. In: *Materials Today: Proceedings* 5.2 (Jan. 2018), pp. 3873–3882. ISSN: 2214-7853. DOI: 10.1016/J.MATPR.2017.11.642.

[7] GE Additive. *Electron Beam Melting*. URL: https://www.ge.com/additive/ebm.

[8] P. Dudek. “FDM 3D printing technology in manufacturing composite elements”. In: *Archives of Metallurgy and Materials* 58.4 (2013), pp. 1415–1418. ISSN: 17333490. DOI: 10.2478/amm-2013-0186.

[9] L. Gonzalez-Macia and A. J. Killard. “Screen printing and other scalable point of care (POC) biosensor processing technologies”. In: *Medical Biosensors for Point of Care (POC) Applications* (2017), pp. 69–98. DOI: 10.1016/B978-0-08-100072-4.00004-6.

[10] Aghnia Ilmiah Nurhudan et al. “Additive manufacturing of metallic based on extrusion process: A review”. In: *Journal of Manufacturing Processes* 66 (June 2021), pp. 228–237. ISSN: 15266125. DOI: 10.1016/j.jmapro.2021.04.018.

[11] Ismail Durgun and Rukiye Ertan. "Experimental investigation of FDM process for improvement of mechanical properties and production cost". In: *Rapid Prototyping Journal* 20.3 (2014), pp. 228–235. ISSN: 13552546. DOI: 10.1108/RPJ-10-2012-0091.

[12] N. A.S. Mohd Pu'ad et al. "Review on the fabrication of fused deposition modelling (FDM) composite filament for biomedical applications". In: *Materials Today: Proceedings* 29 (Jan. 2020), pp. 228–232. ISSN: 2214-7853. DOI: 10.1016/J.MATPR.2020.05.535.

[13] Yvonne Thompson et al. "Fused filament fabrication, debinding and sintering as a low cost additive manufacturing method of 316L stainless steel". In: *Additive Manufacturing* 30 (Dec. 2019), p. 100861. ISSN: 2214-8604. DOI: 10.1016/J.ADDMA.2019.100861.

[14] Bin Liu et al. "Creating metal parts by Fused Deposition Modeling and Sintering". In: *Materials Letters* 263 (Mar. 2020). ISSN: 18734979. DOI: 10.1016/j.matlet.2019.127252.

[15] William D. Callister and David G. Rethwisch. *Material Science and Engineering*. 9th. Wiley, 2015.

[16] Wenzheng Wu et al. "Influence of layer thickness, raster angle, deformation temperature and recovery temperature on the shape-memory effect of 3D-printed polylactic acid samples". In: *Materials* 10.8 (Aug. 2017). ISSN: 19961944. DOI: 10.3390/ma10080970.

[17] Waqar Hassan et al. "The effect of printing parameters on sintered properties of extrusion-based additively manufactured stainless steel 316L parts". In: *The International Journal of Advanced Manufacturing Technology 2021 114:9* 114.9 (Apr. 2021), pp. 3057–3067. ISSN: 1433-3015. DOI: 10.1007/S00170-021-07047-W. URL: https://link.springer.com/article/10.1007/s00170-021-07047-w.

[18] Chanun Suwanpreecha et al. "Influence of Specimen Layout on 17-4PH (AISI 630) Alloys Fabricated by Low-Cost Additive Manufacturing". In: (). DOI: 10.1007/s11661-021-06211-x. URL: https://doi.org/10.1007/s11661-021-06211-x.

[19] S H Masood and W Q Song. "Thermal characteristics of a new metal/polymer material for FDM rapid prototyping process". In: *Thermal characteristics of a new metal/polymer material for FDM rapid prototyping process* (2005). DOI: 10.1108/01445150510626451. URL: www.emeraldinsight.com/researchregister.

[20] Ribin Varghese Pazhamannil, P. Govindan, and P. Sooraj. "Prediction of the tensile strength of polylactic acid fused deposition models using artificial neural network technique". In: *Materials Today: Proceedings* (Feb. 2020). ISSN: 2214-7853. DOI: 10.1016/J.MATPR.2020.01.199.

[21] Damir Godec et al. "Optimization of the 3D Printing Parameters for Tensile Properties of Specimens Produced by Fused Filament Fabrication of 17-4PH Stainless Steel". In: *Materials 2020, Vol. 13, Page 774* 13.3 (Feb. 2020), p. 774. DOI: 10.3390/MA13030774. URL: https://www.mdpi.com/1996-1944/13/3/774/htm%20https://www.mdpi.com/1996-1944/13/3/774.

[22] S. Banerjee and C.J. Joens. "Debinding and sintering of metal injection molding (MIM) components". In: *Handbook of Metal Injection Molding* (Jan. 2019), pp. 129–171. DOI: 10.1016/B978-0-08-102152-1.00009-X.

[23] J. -M. Ting and R. Y. Lin. "Effect of particle size distribution on sintering". In: *Journal of Materials Science 1995 30:9* 30.9 (May 1995), pp. 2382–2389. ISSN: 1573-4803. DOI: 10.1007/BF01184590. URL: https://link.springer.com/article/10.1007/BF01184590.

[24] David Bourell et al. "Materials for additive manufacturing". In: (2017). DOI: 10.1016/j.cirp.2017.05.009. URL: http://dx.doi.org/10.1016/j.cirp.2017.05.009.

[25] D. Taylor. "9.02 - Failure Processes in Hard and Soft Tissues". In: *Comprehensive Structural Integrity* 9 (2007), pp. 35–95. DOI: 10.1016/B0-08-043749-4/09012-1.

[26] Hanpin Lim and Stephen W. Hoag. "Plasticizer effects on physical-mechanical properties of solvent cast Soluplus® films". In: *AAPS PharmSciTech* 14.3 (Sept. 2013), pp. 903–910. ISSN: 15309932. DOI: 10.1208/s12249-013-9971-z.

[27] Variohm Eurosensor Ltd. *What is a Strain Gauge?* URL: https://www.variohm.com/news-media/technical-blog-archive/what-is-a-strain-gauge-.

[28] Instron. *Digital Image Correlation (DIC) Software*. URL: https://www.instron.com/en/products/materials-testing-software/dic-replay?region=Global%20Site&lang=en.

[29] Nick McCormick and Jerry Lord. "Digital Image Correlation". In: *Materials Today* 13.12 (Dec. 2010), pp. 52–54. ISSN: 1369-7021. DOI: 10.1016/S1369-7021(10)70235-2.

[30] M. Azadi et al. "High-cycle bending fatigue properties of additive-manufactured ABS and PLA polymers fabricated by fused deposition modeling 3D-printing". In: *Forces in Mechanics* 3 (Sept. 2021), p. 100016. ISSN: 2666-3597. DOI: 10.1016/J.FINMEC.2021.100016.

[31] Yong Bai and Wei-Liang Jin. "Fatigue Capacity". In: *Marine Structural Design* (2016), pp. 489–507. DOI: 10.1016/B978-0-08-099997-5.00025-3.

[32] N. Pugno et al. "A generalized Paris' law for fatigue crack growth". In: *Journal of the Mechanics and Physics of Solids* 54.7 (July 2006), pp. 1333–1349. ISSN: 0022-5096. DOI: 10.1016/J.JMPS.2006.01.007.

[33] N. E. Dowling, C. A. Calhoun, and A. Arcari. "Mean stress effects in stress-life fatigue and the Walker equation". In: *Fatigue and Fracture of Engineering Materials and Structures* 32.3 (2009), pp. 163–179. ISSN: 8756758X. DOI: 10.1111/J.1460-2695.2008.01322.X.

[34] Ralph I. Stephens et al. *Metal Fatigue in Engineering*. Second Edition. 2001.

[35] Alexander Cochrane. *Ultrafuse 316LX Technical Data Sheet*. Tech. rep. 2017.

[36] BASF. *Safety data sheet*. Tech. rep. 2019, pp. 1–18.

[37] Forward AM. "Ultafuse 316L".

[38] Forward AM. "Debinding Simulation Guidelines for 3D Printed Parts using Ultrafuse ® 316L". URL: www.forward-am.com.

[39] "Prusa Knowledge Base — FAQ - Frequently Asked Questions". URL: https://help.prusa3d.com/en/article/faq-frequently-asked-questions_1932.

[40] GrabCAD. *Prusa i3 MK3S SolidWorks*. 2019. URL: https://grabcad.com/library/prusa-i3-mk3s-solidworks-with-step-1.

[41] "Mettler AG104 204 Balances".

[42] ASTM. "Designation: E8/E8M 21 Standard Test Methods for Tension Testing of Metallic Materials 1". In: (2021). DOI: 10.1520/E0008{_}E0008M-21. URL: www.astm.org,.

[43] ASTM. "Standard Practice for Conducting Force Controlled Constant Amplitude Axial Fatigue Tests of Metallic Materials 1". In: (2022). DOI: 10.1520/E0466-21. URL: www.astm.org,.

[44] ASTM. "Standard Test Method for Measurement of Fracture Toughness 1". In: (2018). DOI: 10.1520/E1820-18. URL: www.astm.org..

[45] Ján Lago et al. "Giga-cycle Fatigue of AISI 316L after Sensitising of Structure". In: *Procedia Engineering*. Vol. 192. Elsevier Ltd, 2017, pp. 528–532. DOI: 10.1016/j.proeng.2017.06.091.

[46] Khairul Azhar Mohammad et al. “Experimental Determination of the Fatigue Behavior of Austenitic 316L Stainless Steel under Fatigue and Creep-Fatigue Tests at High Temperature”. In: *International Journal of Metal and Steel Research Technology* 1.1 (2013), pp. 1–11. URL: http://acascipub.com/Journals.php.

[47] ASM International. “Elements of Metallurgy and Engineering Alloys”. In: (2008). URL: https://www.asminternational.org/documents/10192/1849770/05224G_Chapter14.pdf.

[48] Punit Kumar et al. “Fatigue strength of additively manufactured 316L austenitic stainless steel”. In: *Acta Materialia* 199 (Oct. 2020), pp. 225–239. ISSN: 13596454. DOI: 10.1016/j.actamat.2020.08.033.

A Appendix

SEM images are captured for all fractured fatigue specimens. These images do not directly contribute to new discoveries in the thesis, but they support the conclusions made in Section 5.3.1. The aim of the images is to show potential crack initiation/propagation sites, or other points of interest on the fracture surfaces. The size of the propagation sites is heavily dependent on the stress amplitude and fatigue life, and some images have different magnifications depending on the size. The red square in the overview images (aligned to the left) represents the area for the magnified image (aligned to the right).

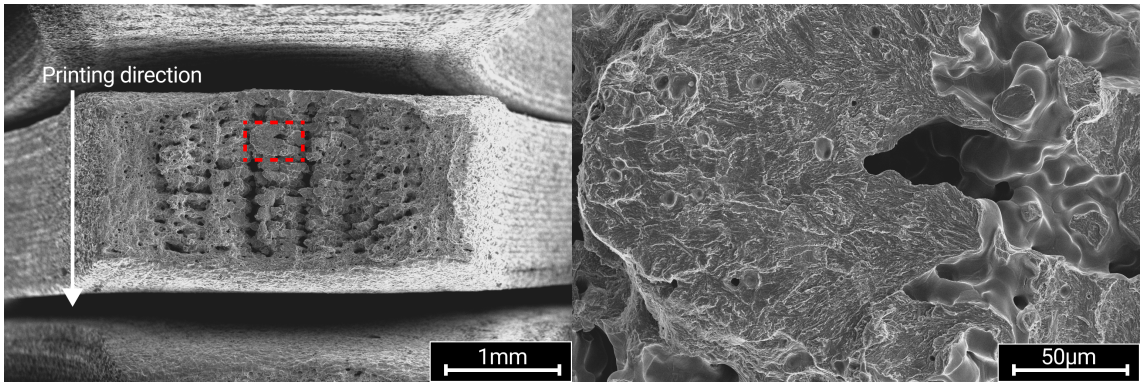

Figure 55: σ_a=150MPa, N_f=40,556 cycles to failure.
40x / 500x magnification. 14.3mm / 14.3mm working distance. 20kV voltage

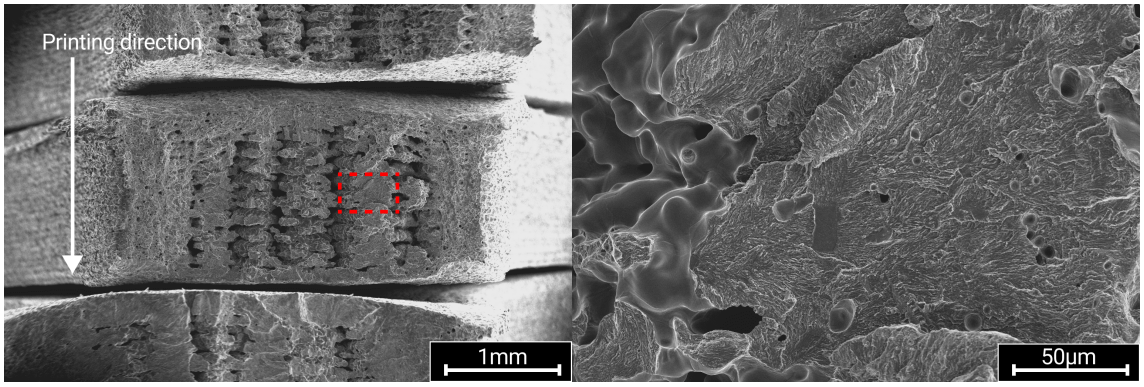

Figure 56: σ_a=150MPa, N_f=87,690 cycles to failure.
40x / 500x magnification. 13.2mm / 13.2mm working distance. 20kV voltage

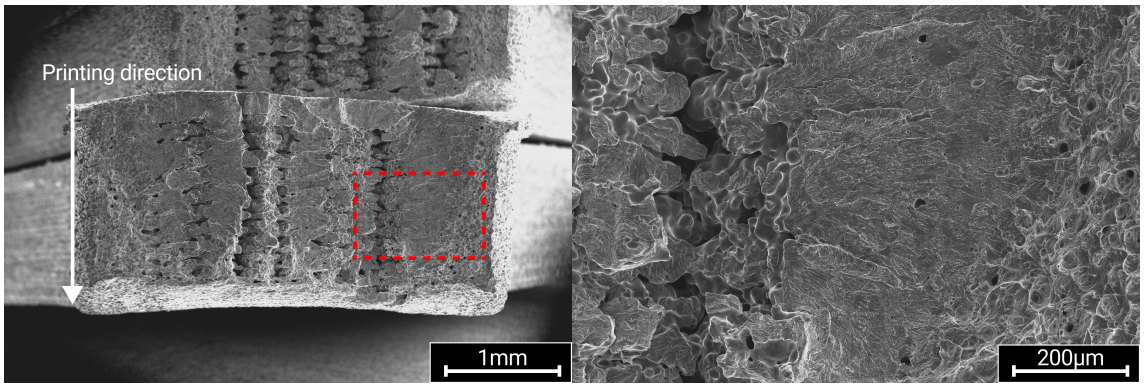

Figure 57: σ_a=130MPa, N_f=30,594 cycles to failure.
40x / 200x magnification. 11.2mm / 11.4mm working distance. 20kV voltage

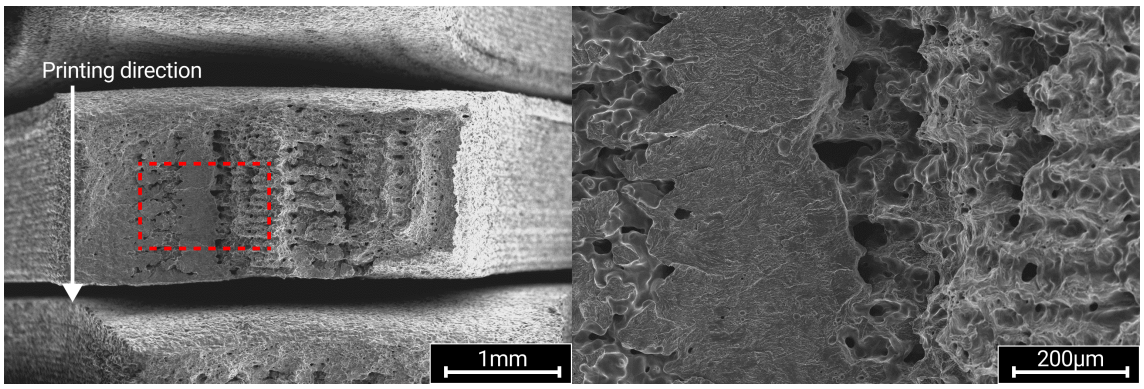

Figure 58: σ_a=130MPa, N_f=69,594 cycles to failure.
40x / 200x magnification. 14.4mm / 15.0mm working distance. 20kV voltage

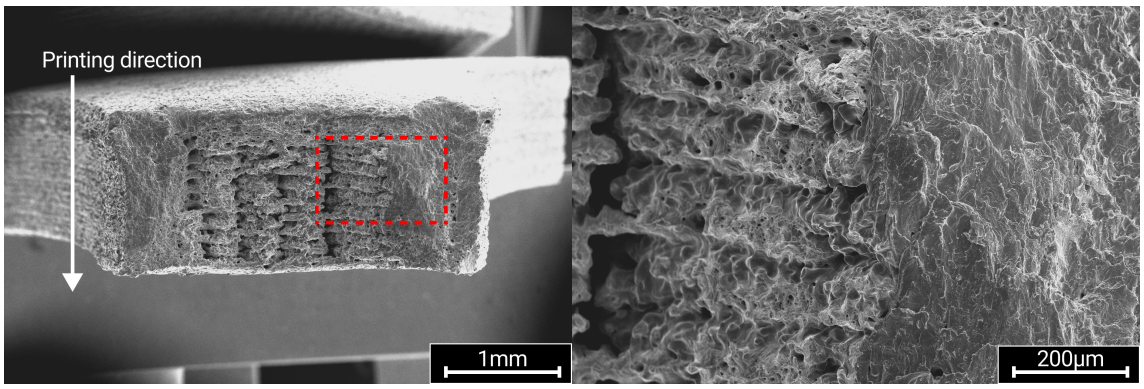

Figure 59: σ_a=120MPa, N_f=241,278 cycles to failure.
40x / 200x magnification. 11.7mm / 11.0mm working distance. 20kV voltage

Figure 60 shows the displacement versus time for each trial of tensile testing. The end-points of the graphs show the fracture points of the specimens.

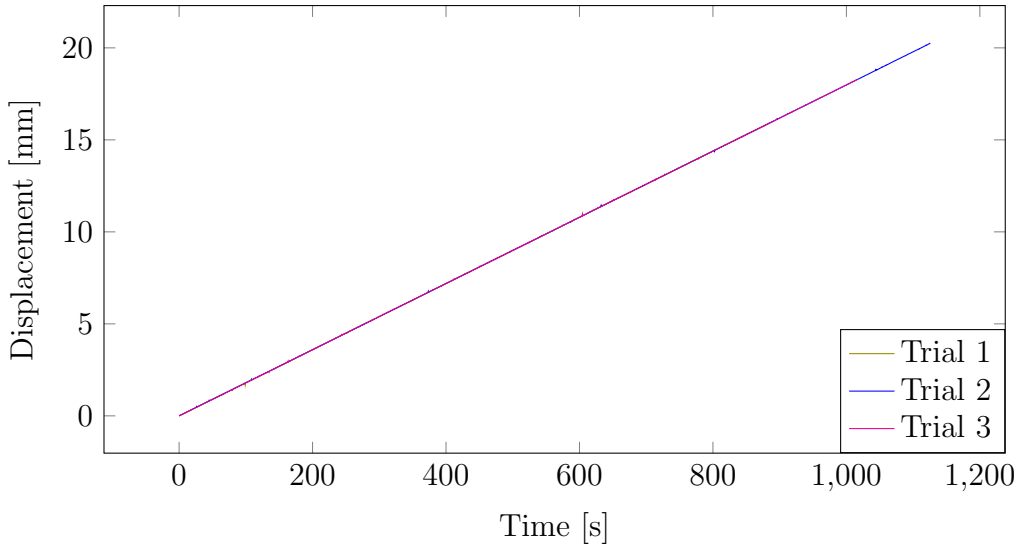

Figure 60: The displacement versus time is shown for three trials of tensile testing.

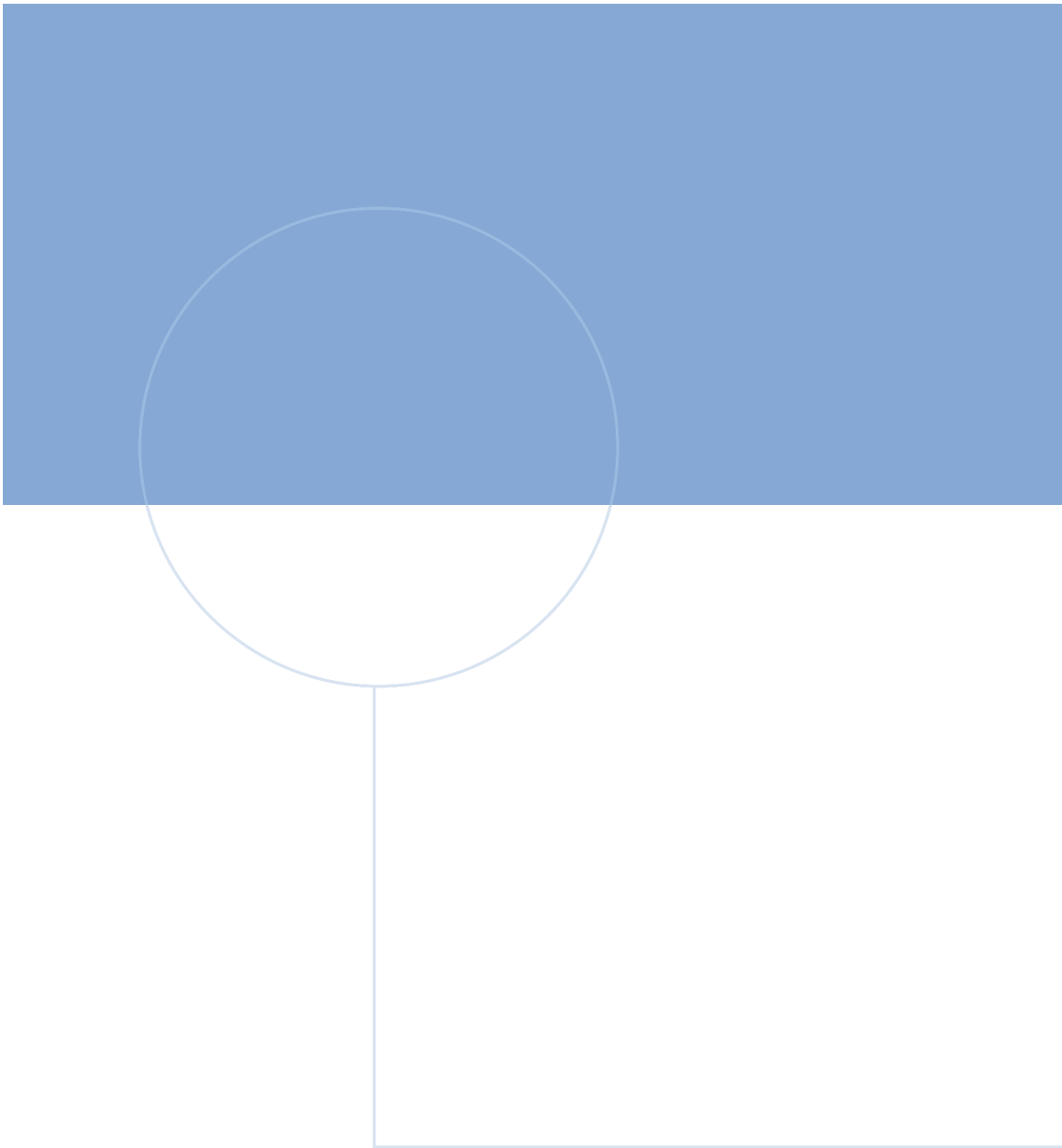

NTNU

Kunnskap for en bedre verden